

Research Article

Detailed Derivation of the Scalar Explicit Expressions Governing the Electric Field, Current Density, and Volumetric Power Density in the Four Types of Linear Divergent MHD Channels Under a Unidirectional Applied Magnetic Field

Osama A. Marzouk 

College of Engineering, University of Buraimi, Al Buraimi, Postal Code 512, Oman
E-mail: osama.m@uob.edu.om

Received: 3 April 2025; **Revised:** 11 May 2025; **Accepted:** 28 May 2025

Abstract: The current study belongs to the field of applied mathematics in plasma physics and electric power, where mathematical analysis of the algebraic equations governing the electric field vector, and the electric-current density field vector within a Magnetohydrodynamic (MHD) linear two-dimensional divergent supersonic channel is utilized to derive analytical expressions for these important fields, as well as closed-form equations for the volumetric power density (output electric power per unit volume of the plasma channel). The expressions presented here describe analytically the operation of the MHD channel as an electric power source within an Open-Cycle Magnetohydrodynamic (OCMHD) generator. The four common types of the MHD linear channels are covered here: namely, (1) continuous-electrode Faraday channel, (2) linear Hall channel, (3) segmented-electrode Faraday channel, and (4) diagonal-electrode channel. The mathematical results, their detailed derivation, and the companion graphical illustrations aid in making a proper decision regarding which channel type is the most suitable for a given application. Under typical operational conditions of 5 S/m plasma electric conductivity, 5 T magnetic field, and 2,000 m/s plasma speed, as well as an optimized load factor of 0.5, we estimate the following numerical values (unsigned magnitudes) for the continuous-electrode Faraday channel (with a Hall parameter of 1): useful electric field (across the external electric load): 5 kV/m, useful electric current-density (between the terminal electrodes within the channel): 12.5 kA/m², volumetric power density (dissipated by the load per unit volume of plasma): 62.5 MW/m³, and electric efficiency (for the electric field or voltage): 50%. For the Hall linear channel (with a Hall parameter of 5), these quantitative performance values become 25 kV/m, 4.808 kA/m², 120.19 MW/m³, and 46.30%. For either an infinitely segmented-electrode Faraday channel or an on-design diagonal-electrode linear channel (and irrespective of the Hall parameter), these quantitative performance values become 5 kV/m, 25 kA/m², 125 MW/m³, and 50%.

Keywords: linear channel, Faraday, Hall, diagonal, magnetohydrodynamic, MHD

MSC: 76W05, 78A55

Abbreviation

β	Hall parameter [dimensionless]
δ	Distance for approximating the gradient [m]
Φ	Electric potential; voltage [V]
γ	Specific heat ratio [dimensionless]
η_{elec}	Electric efficiency [%]
$\eta_{\text{elec}, D}$	Electric efficiency in a diagonal-electrode channel with uniform conditions, when operating at its design point [%]
$\eta_{\text{elec}, F-\text{cont}}$	Electric efficiency in a continuous-electrode Faraday channel with uniform conditions [%]
$\eta_{\text{elec}, F-\text{seg}}$	Electric efficiency in a segmented-electrode Faraday channel with uniform conditions [%]
$\eta_{\text{elec}, H}$	Electric efficiency in a linear Hall channel with uniform conditions [%]
η_{isen}	Isentropic efficiency [%]
μ	Mobility of electrons [(m/s)/(V/m) or m ² /(V.s)]
σ	Electric conductivity [S/m or C/(m.V.s)]
θ_{Φ}	Tilt angle (acute angle, measured from the y-axis) of the equipotential lines [°, degree]
θ_J	Tilt angle (acute angle, measured from the y-axis) of the current-density vector [°, degree]
A	Area [m ²]
B	Unidirectional applied magnetic-field flux density (external magnetic field) [T, tesla]
\vec{B}	The applied magnetic field when expressed as a vector (pointing in the positive z-axis) [T, tesla]
dV	Volume element (for three-dimensional integration) [m ³]
\vec{E}	The electric field within the plasma channel (as felt by the plasma gas) [V/m]
\vec{E}_0	The electric field consumed by the external load [V/m]
\vec{E}_{OC}	The induced open-circuit electric field at the channel electrodes (when no external load is connected) [V/m]
E_x	The axial (x-component) of the internal (within the channel) electric field vector \vec{E} [V/m]
E_{0x}	The axial (x-component) of the electric field outside the channel (as consumed by the external electric load) [V/m]
E_y	The vertical (y-component) of the electric field vector \vec{E} [V/m]
E_{0y}	The vertical (y-component) of the electric field outside the channel (as consumed by the external electric load) [V/m]
E_{OC}	Open circuit (if no external load) induced electric field when approximated as a scalar (unidirectional) quantity. For Faraday-type channels (continuous-electrode Faraday channel or segmented-electrode Faraday channel), $E_{OC} = u B$. For Hall-type channels, $E_{OC} = \beta u B$.
EE	Enthalpy extraction [%]
e	Elementary charge [C]
h	Specific static enthalpy [J/kg]
h_0	Specific total (stagnation) enthalpy [J/kg]
I	Conventional electric current (whose direction is determined assuming positive charge carriers) that flows externally outside the Magnetohydrodynamic (MHD) generator to the electric load [A]
\hat{i}	Unit vector along the positive x-axis [dimensionless]
\vec{J}	Conventional electric current-density vector (whose direction is determined assuming positive charge carriers) within the plasma channel [A/m ²]
J_x	Axial (x-component) of the conventional electric current-density vector \vec{J} [A/m ²]
J_y	Vertical (y-component) of the conventional electric current-density vector \vec{J} [A/m ²]
\hat{j}	Unit vector along the positive y-axis [dimensionless]

K_F	Load factor for Faraday-type channels (continuous-electrode Faraday channel or segmented-electrode Faraday channel) [dimensionless]. This load factor ranges from 0 (short-circuited load) to 1 (open circuit, disconnected load). For either extreme case, the power dissipated by the load is zero (because of having zero voltage drop in the short circuit case, or having zero current flow in the open circuit case). We have $K_F = \frac{R_L}{(R_L + R_G)}$.
K_H	Load factor for Hall-type channels. It ranges from 0 (short-circuited load) to 1 (open circuit, disconnected load) [dimensionless]. For either extreme case, the power dissipated by the load is zero (because of having zero voltage drop in the short circuit case, or having zero current flow in the open circuit case). We have $K_H = \frac{R_L}{(R_L + R_G)}$.
\hat{k}	Unit vector along the positive z -axis [dimensionless]
n_e	Number density of electrons [m^{-3}]
\hat{n}_B	Unit vector along the applied magnetic-field flux density vector [dimensionless]
P	Power density or volumetric power density (output electric power per unit volume of plasma) [W/m^3]
P_D	Output electric power per unit volume of plasma in diagonal-electrode Faraday channels [W/m^3]
$P_{D, \text{opt}}$	Output electric power per unit volume of plasma in diagonal-electrode channels with a matched (optimized) load [W/m^3]
P_F	Output electric power per unit volume of plasma in Faraday channels [W/m^3]
$P_{F-\text{cont}}$	Output electric power per unit volume of plasma in continuous-electrode Faraday channels [W/m^3]
$P_{F-\text{cont, opt}}$	Output electric power per unit volume of plasma in continuous-electrode Faraday channels with matched (optimized) load [W/m^3]
$P_{F-\text{cont, opt, ideal}}$	Output electric power per unit volume of plasma in continuous-electrode Faraday channels with a matched (optimized) load at the limiting case of ($\beta \rightarrow 0$) [W/m^3]
$P_{F-\text{seg}}$	Output electric power per unit volume of plasma in segmented-electrode Faraday channels [W/m^3]
$P_{F-\text{seg, opt}}$	Output electric power per unit volume of plasma in segmented-electrode Faraday channels with a matched (optimized) load [W/m^3]
P_H	Output electric power per unit volume of plasma in linear Hall channels [W/m^3]
$P_{H, \text{opt}}$	Output electric power per unit volume of plasma in linear Hall channels with a matched (optimized) load [W/m^3]
P_{opt}	Output electric power per unit volume of plasma with a matched (optimized) load [W/m^3]
P_w	Output electric power from a magnetohydrodynamic channel [W]
p_0	Total (stagnation) pressure [Pa, N/m^2]
R	Resistance of a solid conductor (in general) [Ω or S^{-1}]
R_L	External resistance (of the load) [Ω or S^{-1}]
R_G	Internal resistance (of the plasma generator) [Ω or S^{-1}]
u	Unidirectional axial plasma bulk speed [m/s]
\vec{u}	The unidirectional axial plasma bulk speed when expressed as a vector (pointing in the positive x -axis) [m/s]

1. Introduction

1.1 Background

Electricity is a main driver for modern civilization [1, 2]. Global electricity generation and demand have been generally increasing steadily since 2000, except for irregularities in 2009 due to the 2008 economic recession and in 2020 due to the COVID-19 pandemic [3–5]. While conventional power systems (i.e., power plants that burn fossil fuels [6–8]) are reliable methods for generating large amounts of electricity, their harmful Greenhouse Gas (GHG) emissions [9–12]

and other pollutants encourage the shift to non-conventional alternatives, such as renewable energy sources (particularly solar energy [13–16] and wind energy [17–19]), and low-carbon hydrogen [20, 21].

Another method for non-conventional electricity generation is the Magnetohydrodynamic (MHD) generator. Such generators utilize the Lorentz force and electromagnetic principles to extract energy from a moving ionized gas (plasma) to produce Direct Current (DC) electricity without rotating or reciprocating elements as found in conventional heat engines [22–24]. The electrically conductive medium in MHD generators can be an ionized gas mixture (plasma) or a liquid metal [25–27]. We here limit ourselves to gas-based MHD generators because we focus on plasma formed from gaseous combustion products [28–30], which is a popular and mature process in fuel-fired thermal power plants.

There are two broad categories of MHD generators. One category of MHD generators is the open-cycle generators, where combustion products (such as carbon dioxide “CO₂” and steam “H₂O”) are seeded with alkaline compounds (e.g., potassium carbonate “K₂CO₃”), and they form weakly-ionized thermal (equilibrium) plasma that is accelerated within a channel while subject to a magnetic field to induce electric fields and electric currents [31, 32]. Such a channel may be viewed as an “electromagnetic turbine”. Being in thermal equilibrium (or thermodynamic equilibrium) means that the electrons (the effective charge carriers due to their light mass and thus high mobility) and the heavy particles in the plasma gas (ions, atoms, and molecules) in such combustion plasmas can be treated as having one common temperature due to the high collision frequencies and high energy transfer per collision [33, 34]. Being open-cycle means that the working plasma is not recirculated back after energy is extracted from it for electricity generation.

The other broad category of MHD generators is the closed-cycle type, in which MHD generators utilize a heated inert gas (e.g., argon “Ar”) [35, 36] whose temperature is elevated using a heat exchanger (rather than a direct combustion process), and this heated gas is seeded with an alkaline metal, such as cesium vapor (Cs) to form a non-equilibrium plasma medium. It should be noted here that the alkali metal cesium, which has an atomic number of 55, vaporizes at a relatively low temperature of about 944 K (671 °C) [37, 38], while it readily melts near room temperatures at only 302 K (29 °C) [39, 40]. Being a non-equilibrium plasma means that its constituent gas particles (electrons, ions, atoms, and molecules) are not in a state of thermal equilibrium, with electrons characterized by a higher temperature compared to heavy particles (ions, atoms, and molecules) [41, 42]. The higher temperature of electrons in inert gas plasmas is necessary for keeping a sufficient level of electric conductivity despite the relatively low bulk temperatures. This state of non-equilibrium (two-temperature plasma) can be achieved by ohmic heating (Joule heating) under a relatively small frequency of collisions between the electrons and the neutral gas atoms [43, 44]. Being closed-cycle means that the working plasma is recirculated back after energy is extracted from it for electricity generation. Before repeating the energy extraction process, energy is added again to the depleted plasma (e.g., by a heat exchanger) to restore its initial state [45].

Closed-Cycle Magnetohydrodynamic (CCMHD) generators typically have a disc shape [46–50], and this design allows efficient utilization of the magnets [51]. The compactness of CCMHD generators renders them of special interest in space applications, especially in space missions reaching trajectories far from the sun, where solar irradiation and photovoltaic power conversion become ineffective [52].

On the other hand, Open-Cycle Magnetohydrodynamic (OCMHD) generators pertain more to terrestrial electricity generation, where they can provide much larger production capacities similar to utility-scale power plants that use an open (non-recirculating) Brayton cycle or a closed (circulating) Rankine cycle [53–55]. Such OCMHD generators may be used either in a continuous mode as power plants or in a pulsed mode for geological prospecting (like the Sakhalin 510 MW unit [56, 57]).

In a recent review study of MHD power generation, one of the mentioned advantages of OCMHD was the ability to work at very high temperatures (such as 2,800 K) that are well beyond what conventional turbines of any type can tolerate. From the Carnot efficiency condition in thermodynamics [58, 59], such higher temperatures theoretically mean that higher thermal efficiencies of energy conversion are possible, provided that the plasma can be exploited to near ambient temperatures. That review study also referred to a number of technical challenges for MHD power generation, which included improving the scalability of that MHD technology [60].

The performance of MHD generators can be described in terms of three percentage metrics [61, 62].

First, we have the enthalpy extraction or Enthalpy Extraction ratio (*EE*) metric, which is the ratio of the drop in static enthalpy (Δh) within the MHD generator to the inlet static enthalpy (h_{in}) at the entrance of the MHD generator. Thus,

$$EE = \frac{\Delta h}{h_{in}} = 1 - \frac{h_{out}}{h_{in}} \quad (1)$$

where (h_{in}) and (h_{out}) are the specific static enthalpy (which is a thermodynamic property that expresses energy content per unit mass of a fluid medium [63]) of the plasma at the entrance and at the exit of the MHD generator. A high Enthalpy Extraction (EE) of 38% was successfully demonstrated experimentally for a disc-type MHD generator [64].

Second, there is the MHD generator isentropic efficiency (η_{isen}) [65], which relates the actual relative drop in the static enthalpy to the ideal relative drop in the total (stagnation) enthalpy (h_0) in the case of an isentropic process under the assumption of a calorically-perfect gas (thus, having constant specific heat capacities and constant specific heat ratio) [66–68]. This MHD isentropic efficiency is

$$\eta_{isen} = \frac{\frac{\Delta h}{h_{in}}}{\frac{\Delta h_0}{h_{0, in}}} \quad (2)$$

where $(h_{0, in})$ is the specific total or stagnation (which refers to the hypothetical condition when the fluid becomes at rest [69, 70]) enthalpy of the plasma at the entrance of the MHD generator.

The above equation can be written in terms of the total pressure (the stagnation pressure, which is the sum of the static pressure and the dynamic pressure [71, 72]) at the entrance of the MHD generator ($p_{0, in}$) and at the exit of the MHD generator ($p_{0, out}$) using standard expressions for isentropic compressible calorically-perfect flows [73] as

$$\eta_{isen} = \frac{\frac{\Delta h}{h_{in}}}{1 - \left(\frac{p_{0, out}}{p_{0, in}} \right)^{\frac{\gamma-1}{\gamma}}} \quad (3)$$

where (γ) is a constant specific heat ratio (ratio of the specific heat capacity at constant pressure to the specific heat capacity at constant volume [74, 75], and it is also called the adiabatic index [76]). A high MHD isentropic efficiency (η_{isen}) of 63% was successfully demonstrated experimentally for a disc-type MHD generator [77].

Third, there is the MHD generator electric (η_{elec}), which is defined as the ratio of the electric power to the mechanical power. Mathematically, this is expressed as

$$\eta_{elec} = \frac{-\iiint_{\text{volume}} \vec{J} \cdot \vec{E}_0 dV}{-\iiint_{\text{volume}} \vec{u} \cdot (\vec{J} \times \vec{B}) dV} \quad (4)$$

Open-Cycle Magnetohydrodynamic (MHD) generators are primarily in the form of a linear channel, in which the weakly-ionized plasma moves at a high speed while subject to a strong applied magnetic field [78]. The inlet plasma speed can be subsonic ($\text{Mach} < 1$) [79, 80] or supersonic ($\text{Mach} > 1$) [81–84]. Contrary to subsonic and incompressible flows [85, 86], supersonic flows at the MHD channel entrance need a divergent MHD channel in order to allow the supersonic flow to expand and accelerate [87–89]. Attached electrodes are used to transmit the collected electric current to an external electric load. There are four common designs for the open-cycle MHD channels; namely, (1) continuous-electrode Faraday channel [90–92], (2) segmented-electrode Faraday channel [93–95], (3) linear Hall channel (always have segmented electrodes) [96–98], and (4) diagonal channel or diagonal-electrode channel or diagonally-shortened channel

(always have segmented electrodes) [99–101]. Each of these designs has a unique layout of its electrodes, hence the name of its type.

1.2 Goal of the study

This work can be viewed as an extension of our earlier studies about mathematical modeling for Magnetohydrodynamic (MHD) power generation. We previously presented the governing electric equations in the MHD channel under various levels of modeling approximation [102]. We also presented a proposed mathematical model for relating the electric conductivity of MHD plasma to its local temperature, pressure, and chemical composition [103].

In continuation of our work about mathematical modeling for Magnetohydrodynamic (MHD) generators, we here aim to present mathematical expressions for the electric field and electric current-density field within the plasma of an open-cycle MHD generator, and the resulting output power density under the four types of linear MHD channels. We supplement the mathematical analysis with illustrative sketches and logical derivation starting from elementary equations.

1.3 Benefits of the study

Our review of the mathematical expressions for linear Magnetohydrodynamic (MHD) generator channels, our organized presentation, and contrasting have a number of benefits. First, it serves as an introductory guide for readers interested in Open-Cycle MHD (OCMHD) power generation and the differences in their performance according to the different channel configurations. Second, our review provided here involves explicit algebraic scalar expressions, enabling parametric and visual investigation of the influence of some parameters on various variables of importance in the OCMHD channel. For example, the penalty in the electric output power density (P) due to the Hall parameter (β) in the case of a continuous-electrode Faraday channel can be easily identified through the presented mathematical expressions in the current study. Third, the directions of the vector fields under each channel configuration are clarified, and this is particularly useful in understanding the operation of the MHD generator for each case by a reader who is not an expert in plasma physics and MHD power generation. Fourth, the analytical treatment presented here facilitates optimizing the performance. For example, the load factor in the linear Hall channel can be optimized for maximum power output through the presented mathematical expressions in this study. Fifth, this study can be used in its exact form or can be modified and integrated with teaching materials or projects for enriching undergraduate academic courses in plasma physics, plasma applications, energy systems, and electrical power generation; and this can improve the conceptual understanding of students [104].

2. Research method

The method followed in the current study is the symbolic mathematical manipulation of a fundamental generic equation for electrically conducting moving plasma. This equation is the generalized (extended) Ohm's law in its vector form, which accounts for the Hall effect (Hall current-density) as well as the electromagnetic induction effect (Faraday current-density).

We expand this vector equation into three scalar equations (corresponding to the three Cartesian components). Then, we apply our assumptions to deduce two scalar equations for the axial component (along the plasma's travel direction) and the vertical components (perpendicular to the magnetic field and the plasma velocity). We drop the third scalar equation (in the direction of the magnetic field) because it becomes trivial in our case.

These two derived scalar equations are analyzed further for each of the four linear channel configurations; and this leads to the aimed mathematical expressions for the electric field, electric current-density, and power density for each configuration.

The common assumptions made in this study are:

The MHD channel has a divergent geometry, with a trapezoidal cross-section (in the $x - y$ plane). Such a simple MHD channel has been realized in the Sakhalin pulsed MHD generator [105]. The width (along the magnetic field) is constant, and its influence is disregarded here (this is equivalent to assuming infinite width, thus two-dimensional channels).

- The charge carriers are only the free electrons in the plasma (liberated as a result of thermal ionization). This means that while ions also exist (to ensure the overall neutrality of the plasma), their contribution to the electric current is neglected [106, 107]. This is a reasonable assumption given the much stronger mobility of the lighter electrons compared to the heavier ions [108–110].

- Unidirectional magnetic field (magnetic-field flux density) that points in the positive z -axis. Therefore, the magnetic-field flux density vector (\vec{B}) can be expressed as $B \hat{k}$, where (\hat{k}) is a unit vector in the direction of the positive z -axis. Because the magnetic field is externally applied, this assumption can be justified. In such a case, special electromagnetic designs can be made to approximate this assumption. This treatment of the magnetic field as being fully controllable implies a low magnetic Reynolds number assumption [111–114], where auxiliary induced magnetic-field flux density due to the moving plasma (the self-excitation phenomenon) is neglected [115–118]. This “inductionless” assumption [119–121] of a low magnetic Reynolds number is reasonable for MHD generators [122–124].

- Unidirectional plasma velocity that points in the positive x -axis. Therefore, the plasma velocity vector (\vec{u}) can be expressed as $u \hat{i}$, where (\hat{i}) is a unit vector in the direction of the positive x -axis. Although this assumption neglects turbulence and no-slip effects in the plasma flow, it can be regarded as an acceptable treatment for deriving system-level laws, where the time-averaged bulk velocity of the plasma should be primarily in the axial direction. This assumption becomes more valid when the divergence angle of the channel decreases, so the channel height approaches uniformity. In addition, turbulence tends to be suppressed as the Mach number increases [125, 126], and our study is for supersonic channels. In addition, adopting a one-dimensional approximation for a channel flow or exterior flow has been implemented in other studies [127–130].

- No electric field along the lateral direction (along the direction of the magnetic field). This assumption is aligned with the unidirectionality assumption for the magnetic field. Even if the plasma has a three-dimensional flow velocity, the unidirectional magnetic field along the z -axis is not able to induce an electric field in the same z -direction. Therefore, the electric field along the z -axis within the MHD plasma can only be caused by an externally applied electric field, but such a case is not considered in the current study, where there are no electrodes along the z -axis to permit this.

3. Results

In this section, we present a detailed derivation of scalar mathematical equations that describe various performance aspects of four types of linear MHD channels. We start with a common preparatory subsection, and then dedicate one subsection to each of the four channels. Therefore, the current section is divided into five subsections.

3.1 Base scalar equations for electric fields in MHD plasma

In this subsection, we derive the two base scalar equations for the conventional electric current-density and the load-consumed electric field, under the assumptions made in the previous section, particularly the unidirectional magnetic field and the unidirectional plasma velocity. These scalar equations are the x -component and the y -component of the generalized Ohm’s law, which applies to a three-dimensional conductor medium (rather than a conductive wire).

The generalized Ohm’s law (for plasma with neglected ion drift) relates the electric current-density (\vec{J}) to the electric field (\vec{E}), electric conductivity (σ), and the applied magnetic field (\vec{B}) [131–133]. It should be noted that we adopt the conventional current here, rather than the electron current [134–136]. The only difference if the electron current is adopted rather than the conventional current is that the electric current-density (\vec{J}) should have a minus sign in each appearance for it in our presented mathematical formulations.

The generalized Ohm’s law can be expressed in different forms. We start with the following convenient form for it, which facilitates our discussion and subsequent analysis:

$$\vec{J} = \sigma \vec{E} - \mu \vec{J} \times \vec{B} \quad (5)$$

where (μ) is the electron mobility.

The Hall parameter (β) is the electron mobility (μ) divided by the magnitude of the applied magnetic-field flux density (B). Mathematically, this is expressed as

$$\mu = \frac{\beta}{B} \quad (6)$$

It is useful to add here that the electric conductivity of the plasma (σ) due to the free electrons (ions contribution is neglected as mentioned earlier) is [137–139]

$$\sigma = e n_e \mu \quad (7)$$

where (n_e) is the number density of the charge-carrier electrons, and (e) is the elementary charge (the absolute electric charge of an electron; $e = 1.6021766 \times 10^{-19} \text{ C}$ [140–142]).

Therefore, the generalized Ohm's law form in Equation (5) can be expressed in an alternative form as

$$\vec{J} = \sigma \vec{E} - \beta \vec{J} \times \hat{n}_B \quad (8)$$

where (\hat{n}_B) is a unit vector in the direction of the applied magnetic-field flux density vector (\vec{B}). Thus, this unit vector is defined as

$$\hat{n}_B \equiv \frac{\vec{B}}{B} \quad (9)$$

The first term in Equation (8), the term ($\sigma \vec{E}$), is an extended version of the classical Ohm's law for a one-dimensional solid conductor. To demonstrate this; one can multiply both sides of the equation by the area (A) perpendicular to the electric current-density, and then replace the vector electric field (\vec{E}) by the negative value of the scalar gradient of the electric potential (Φ). This gives

$$J A = \sigma A \left(-\frac{\Delta \Phi}{\delta} \right) \quad (10)$$

where (J) is the magnitude of the unidirectional current density; (δ) is the separation distance between the two electrodes; and $\left(-\frac{\Delta \Phi}{\delta} \right)$ is a numerical approximation for the gradient of the electric potential (Φ), and it becomes exact in the case of a linear decrease of the electric potential in the direction of the conventional electric current density.

The product ($J A$) in the above equation is the electric current (I).

$$I = J A \quad (11)$$

Also, the quantity $\left(\frac{\sigma A}{\delta}\right)$ is the reciprocal of the resistance (R) of the conductor. Therefore,

$$R = \frac{\delta}{\sigma A} \quad (12)$$

Using Equation (11) and Equation (12) in Equation (10) gives the classical Ohm's law, as

$$I = -\frac{\Delta\Phi}{R} \quad (13)$$

The minus sign in the above equation indicates that the electric potential drops in the direction of the electric current. This minus sign is normally dropped when Ohm's law is expressed, with the understanding that the electric potential drops across the conductor or the load.

The second term in Equation (8), the term $(-\beta \vec{J} \times \hat{n}_B)$, is the Hall electric current-density due to the Hall effect, where an electric voltage is induced as a result of the movement of the electrons under the effect of the applied magnetic field, and this leads to a "secondary" Hall current density perpendicular to both the "primary" current density (\vec{J}) and the applied magnetic field (\vec{B}) [143–145]. The magnitude of this "secondary" or Hall current density, $|\beta \vec{J} \times \hat{n}_B|$, is proportional to the Hall parameter (β). Thus, from Equation (6), The magnitude of this "secondary" or Hall current density, $|\beta \vec{J} \times \hat{n}_B| = |\mu B \vec{J} \times \hat{n}_B|$, is proportional to either the magnitude of the applied magnetic field (B) or the electron mobility (μ).

In the current study, the applied magnetic-field flux density vector is assumed to be totally in the direction of the z -axis, whose unit vector is (\hat{k}). Therefore, we have

$$\hat{n}_B = \hat{k} \quad (14)$$

Using Equation (14) in Equation (8) gives a third form for the generalized Ohm's law, which is

$$\vec{J} = \sigma \vec{E} - \beta \vec{J} \times \hat{k} \quad (15)$$

The cross product $(\vec{J} \times \hat{k})$ leads to a vector that has two non-trivial components along the x -axis and y -axis only, as

$$\vec{J} \times \hat{k} = (J_x \hat{i} + J_y \hat{j} + J_z \hat{k}) \times \hat{k} = -J_y \hat{i} + J_x \hat{j} \quad (16)$$

Using Equation (16) in Equation (15), and collecting terms for the three Cartesian components gives the following three scalar equations:

$$J_x = \sigma E_x - \beta J_y \quad (17)$$

$$J_y = \sigma E_y + \beta J_x \quad (18)$$

$$J_z = \sigma E_z \quad (19)$$

Given that the z -component of the within-channel electric field vector (\vec{E}) is zero here

$$E_z = 0 \quad (20)$$

then, Equation (19) implies also that the z -component of the electric current-density is zero

$$J_z = 0 \quad (21)$$

Equation (17) and Equation (18) are implicit expressions for the x -component and the y -component of the electric current-density, and these two components (J_x and J_y) are clearly coupled. However, these two coupled equations can be solved simultaneously to obtain two explicit uncoupled expressions for these two components (J_x and J_y), with the result being as follows:

$$J_x = \frac{\sigma}{1 + \beta^2} (E_x - \beta E_y) \quad (22)$$

$$J_y = \frac{\sigma}{1 + \beta^2} (E_y + \beta E_x) \quad (23)$$

The electric field vector within the plasma (\vec{E}) is the vector sum of the electric field source vector or the open-circuit electric field vector (\vec{E}_{OC}) that is induced due to the motion of the electrically-conductive plasma under the effect of the applied magnetic field vector, and the electric field sink (\vec{E}_0) that is consumed by the external electric load (if a load is connected). Thus,

$$\vec{E} = \vec{E}_0 + \vec{E}_{OC} \quad (24)$$

The load electric field (\vec{E}_0) in MHD power generation is dependent on the connected load. However, if the MHD channel is used in a reverse mode as a plasma accelerator (a magnetohydrodynamic drive), then this electric field (\vec{E}_0) can be then viewed as an applied one, and the electric current is applied to the MHD electrodes from a powerful external Direct Current (DC) source, rather than being collected from the MHD electrodes [146–148].

The induced or convection open-circuit electric field vector (\vec{E}_{OC}) is related to the bulk velocity of the plasma (\vec{u}) and the applied magnetic field vector (\vec{B}), while being perpendicular to both of them [149, 150]. Thus,

$$\vec{E}_{OC} = \vec{u} \times \vec{B} \quad (25)$$

From the two previous equations, Equation (24) and Equation (25), we can write the following:

$$\vec{E} = \vec{E}_0 + \vec{u} \times \vec{B} \quad (26)$$

For our case of a unidirectional magnetic field ($\vec{B} = B \hat{k}$) and unidirectional convective plasma velocity ($\vec{u} = u \hat{i}$), the x -component and the y -component of the above vector equation are

$$E_x = E_{0x} \quad (27)$$

$$E_y = E_{0y} - u B \quad (28)$$

Using the above two expressions for (E_x) and (E_y) in Equation (22) and Equation (23) gives

$$J_x = \frac{\sigma}{1 + \beta^2} (E_{0x} - \beta E_{0y} + \beta u B) \quad (29)$$

$$J_y = \frac{\sigma}{1 + \beta^2} (E_{0y} - u B + \beta E_{0x}) \quad (30)$$

These two scalar expressions are to be analyzed further, and their customized form is to be discussed for each case of the four designs of the linear Magnetohydrodynamic (MHD) channels. This is presented in the next four subsections, with one subsection dedicated to each channel design.

In the case of Faraday-type MHD linear channels (the continuous-electrode version or the segmented-electrode version), it is the y -component of the current density (J_y) and load electric field (E_{0y}) that are useful because these are the current densities effectively collected by the channel electrodes (the anode and cathode, which are separated vertically “along the y -axis”). In such cases, a Faraday load factor (K_F) can be introduced as the ratio of the load electric field (E_{0y}) to the induced electric field ($u B$). So, mathematically, we have

$$K_F \equiv \frac{E_{0y}}{u B} \quad (31)$$

Equivalently, this Faraday load factor can be viewed as the ratio of the electric resistance of the load (R_L) to the total series resistance encountered by the electric current flow due to both the external electric resistance of the load and the effective internal electric resistance within the MHD generator itself, that is designated by the symbol (R_G) (this internal resistance is caused by the bulk plasma region, the boundary layer near the wall [151, 152], and any solid slag layer formed on the electrodes [153–156]). Therefore, the Faraday load factor (K_F) can be mathematically described as

$$K_F \cong \frac{R_L}{R_L + R_G} \quad (32)$$

Therefore, the Faraday load electric field (E_{0y}) can be expressed as

$$E_{0y} = K_F u B \quad (33)$$

The value of (K_F) is bounded between 0 and 1. In the extreme condition of $K_F = 1$, the circuit is open (the external load is disconnected). This corresponds to setting the load resistance to infinity ($R_L = \infty$) in Equation (32). At the other extreme condition of $K_F = 0$, the circuit is shorted (the external load is replaced with a perfect electric conductor). This corresponds to setting the load resistance to zero ($R_L = 0$) in Equation (32). It can be shown that maximum power delivery to the “matched” external load occurs at an optimum Faraday load factor of $K_F = 0.5$ [157].

In general, the Direct Current (DC) electric power delivered to the load powered by a magnetohydrodynamic channel is [158]

$$P_w = - \iiint_{\text{volume}} \vec{J} \cdot \vec{E}_0 dV \quad (34)$$

where (dV) is an infinitesimal volume element.

The Direct Current (DC) electric power delivered to the load in the case of a Faraday-type MHD generator per unit volume of plasma is

$$P_F = E_{0y} |J_y| = K_F u B |J_y| \quad (35)$$

where $|J_y|$ is the absolute value of the vertical “i.e., parallel to the y -direction” current density (since it actually has a negative value due to pointing in the negative y -direction).

In the case of Hall-type linear MHD channels, it is the x -component of the current density (J_x) and load electric field (E_{0x}) that are useful because these are the current densities effectively collected by the channel electrodes (the anode and cathode, which are separated axially “along the x -axis”). In such cases, a Hall load factor (K_H) can be introduced as the ratio of the load electric field (E_{0x}) to the induced (open circuit) axial electric field ($\beta u B$). So, mathematically, we have

$$K_H \equiv \frac{|E_{0x}|}{\beta u B} \quad (36)$$

where $|E_{0x}|$ is the absolute value of the axial load electric field (since it is actually having a negative value due to pointing in the negative x -direction).

As in the case of the Faraday load factor, the Hall load factor can be viewed as the ratio of the electric resistance of the load (R_L) to the total series resistance encountered by the electric current flow due to both the external electric resistance of the load and the effective internal electric resistance within the MHD generator itself (R_G). Therefore, the Hall load factor (K_H) can be mathematically described as

$$K_H \cong \frac{R_L}{R_L + R_G} \quad (37)$$

Therefore, the absolute value of the Hall load electric field ($|E_{0x}|$) can be expressed as

$$|E_{0x}| = K_H \beta u B \quad (38)$$

As in the case of the Faraday load factor, the value of (K_H) is bounded between 0 and 1. In the extreme condition of $K_H = 1$, the circuit is open. At the other extreme condition of $K_H = 0$, the circuit is shorted. Maximum power delivery to the “matched” external load occurs at an optimum Hall load factor of $K_H = 0.5$ [159].

The Direct Current (DC) electric power delivered to the load in the case of a linear Hall MHD generator per unit volume of plasma is

$$P_H = |E_{0x}| J_x = K_H \beta u B J_x \quad (39)$$

3.2 Continuous-electrode Faraday channel

The first MHD channel design we review in this study is the continuous-electrode Faraday configuration. This is the simplest configuration among the four linear MHD channels in terms of physical construction and electric connectivity.

Using Equation (33) in Equation (29) and Equation (30) gives a customized form for the electric current-density components suitable for Faraday-type channels as

$$J_x = \frac{\sigma}{1+\beta^2} (E_{0x} - \beta K_F u B + \beta u B) = \frac{\sigma}{1+\beta^2} (E_{0x} + \beta u B [1 - K_F]) \quad (40)$$

$$J_y = \frac{\sigma}{1+\beta^2} (K_F u B - u B + \beta E_{0x}) = \frac{\sigma}{1+\beta^2} (\beta E_{0x} - u B [1 - K_F]) \quad (41)$$

In Figure 1, we illustrate the geometric layout of this channel in the $x - y$ plane. The top side represents the anode electrode, which has a negative (or grounded) polarity. The bottom side represents the cathode electrode, which has a positive polarity. In this sketch, the channel height (the separating distance between the two electrodes) is assumed to increase linearly with the axial distance (x). This is not necessary, and nonlinear profiles are permitted as well [160]. However, in the shown linearly-divergent channel, the equipotential surfaces (the virtual surfaces with constant electric potential Φ) become flat planes (straight lines in the shown two-dimensional sketch). These potential planes are projected in the $x - y$ plane as inclined straight lines, with their inclination gradually change from being coincident with the anode at the top to being coincident with the cathode at the bottom. In our sketch, we provide arbitrary values for sample intermediate equipotential lines, in addition to the top anode (which is also an equipotential line), and the bottom cathode (which is an equipotential line). We assign an electric potential of 30 V to the cathode, and a reference zero potential to the anode. These are not realistic values because they are small (actual cathode potential can exceed hundreds of volts [161–163]), but they are provided just to improve the explanation through numerical examples.

The y -component of the load electric field (E_{0y}) is positive in the case of the continuous-electrode Faraday channel, meaning that it is pointing vertically up, from the bottom positive cathode to the top negative (or grounded reference) anode. The load electric field vector is in the direction of decreasing electric potential [164–166], and this justifies the upward direction of (E_{0y}).

We also repeat below the general expression for (E_{0y}) for Faraday-type channels, which was presented earlier (Equation (33)).

If the MHD channel is uniform in height (no geometric divergence), then the condition $(E_{0x} = 0)$ becomes applicable locally, not just at an integrated level.

Thus, the overall load electric field is effectively upward (from the bottom cathode to the top anode).

The absolute value of the local acute inclination angle (θ_Φ) of the equipotential line (measured from the “vertical” y -axis) is determined from the local values of the absolute x -component and the y -component (always positive here) of the load electric field; namely $(|E_{0x}|)$ and (E_{0y}) , respectively. Therefore, mathematically, we have

$$\theta_\Phi = \tan^{-1} \left(\frac{E_{0y}}{|E_{0x}|} \right) \quad (43)$$

For example, the centerline equipotential line is exactly horizontal, thus the local load electric field vector is exactly vertical (thus, $|E_{0x}| = 0$). Therefore, the centerline equipotential line has

$$\theta_\Phi = \tan^{-1} \left(\frac{E_{0y}}{|0|} \right) = \tan^{-1}(\infty) = 90^\circ \quad (44)$$

Applying the condition $(E_{0x} = 0)$ to the two base equations, Equation (40) and Equation (41), gives the following two customized relations for the electric current-density vectors in the case of the continuous-electrode Faraday channel:

$$J_x = \frac{\sigma}{1 + \beta^2} \beta u B (1 - K_F) \quad (45)$$

$$J_y = -\frac{\sigma}{1 + \beta^2} u B (1 - K_F) \quad (46)$$

Since the values of (σ) , (β) , (u) , (B) , and $(1 - K_F)$ in the above equation are positive; the two previous equations imply that the x -component of the current density (J_x) is positive, while the y -component of the current density (J_y) is negative. Therefore, the electric current-density vector (\vec{J}) in the case of the continuous-electrode Faraday channel is inclined right down. Furthermore, the magnitude of this inclination angle (θ_J) , which is the acute angle measured from the vertical y -axis, is governed by

$$\theta_J = \tan^{-1} \left(\frac{J_x}{|J_y|} \right) \quad (47)$$

However, it can be seen from Equation (45) and Equation (46) that the ratio $\left(\frac{J_x}{|J_y|} \right)$ reduces to the Hall parameter (β) . Therefore

$$\theta_J = \tan^{-1}(\beta) \quad (48)$$

Because the Hall parameter (β) depends on the electron mobility, which in turn depends on the local chemical composition, the temperature, and the pressure of the plasma gas [167–169]; the direction of the current density vectors

(\vec{J}) may change spatially from one point to another within the MHD channel (but still pointing in the right-down direction). In the special case of uniform isothermal plasma, the value of (β) becomes constant throughout the MHD channel, and thus the electric field vectors (\vec{J}) become parallel.

From Equation (35), the Direct Current (DC) electric power delivered to the load in the case of the continuous-electrode Faraday channel per unit volume of plasma ($P_{F-\text{cont}}$) is

$$P_{F-\text{cont}} : K_F u B |J_y| = K_F u B \frac{\sigma}{1+\beta^2} u B (1-K_F) = \frac{\sigma}{1+\beta^2} u^2 B^2 K_F (1-K_F) \quad (49)$$

When the above expression is optimized with respect to the Faraday load factor (K_F), the optimum case occurs at ($K_F = 0.5$). This means that the external resistance of the matched (optimized) load is equal to the internal resistance of the MHD generator, or

$$R_{L, \text{opt-F}} = R_G \quad (50)$$

In such a case of ($K_F = 0.5$), the matched-load optimized power dissipation to the load (per unit plasma volume) in the continuous-electrode Faraday channel is

$$P_{F-\text{cont, opt}} = 0.25 \frac{1}{1+\beta^2} \sigma u^2 B^2 \quad (51)$$

The factor $\left(\frac{1}{(1+\beta^2)}\right)$ in the above equation represents a power penalty due to the uncollected “parasitic” Hall current density (J_x).

In the limiting case of zero Hall effect ($\beta = 0$), the above expression for the optimized load power (per unit plasma volume) becomes

$$P_{F-\text{cont, opt, ideal}} = 0.25 \sigma u^2 B^2 \quad (52)$$

However, practically, this ideal condition is not achievable with the continuous-electrode Faraday channel, because the theoretical condition that ($\beta = 0$) also implies zero electron mobility ($\mu = 0$) according to Equation (6). From Equation (7), such a condition implies zero electric conductivity ($\sigma = 0$), and thus the MHD generator ceases to produce electricity.

The inevitable Hall effect loss associated with the continuous-electrode Faraday channel is a major disadvantage, making this channel type suitable only for a restricted regime of low (β). For example, at a Hall parameter value of ($\beta = 0.5$), 20% of the ideal power limit is lost, which is a reasonable loss; while at a Hall parameter of ($\beta = 1$), 50% of the ideal power limit is lost; and at a Hall parameter of ($\beta = 2$), 80% of the ideal power limit is lost and this is high. All these three values of (β) are possible in open-cycle MHD generator plasma [170]. The use of continuous-electrode Faraday channel may be regarded as acceptable up to a limit of approximately ($\beta = 2$) [171].

To avoid the aforementioned power loss problem, alternative MHD channel designs should be used, and this leads to the three alternative configurations of linear MHD channels to be discussed in the next three subsections.

We conclude this subsection by deriving an expression for the electric efficiency of the continuous-electrode Faraday channel. From the general expression in Equation (4), a reduced version can be obtained if the channel has uniform electromagnetic properties, and this reduced form is

$$\eta_{\text{elec}, F-\text{cont}} = \frac{|J_x E_{0x}| + |J_y E_{0y}|}{u |J_y| B} = \frac{|J_y| E_{0y}}{u |J_y| B} = \frac{E_{0y}}{u B} = \frac{K_F u B}{u B} = K_F \quad (53)$$

Thus, the electric efficiency reduces to the Faraday load factor (K_F) in the case of a continuous-electrode Faraday channel with uniform properties. This also means that the optimum electric efficiency ($\eta_{\text{elec}, F-\text{cont}, \text{opt}}$) in this channel configuration is 0.5 or 50%.

3.3 Linear Hall channel

After discussing the operation of the continuous-electrode Faraday MHD channel in the previous subsection, and highlighting the deficiency caused by the Hall effect in that type of linear MHD channels, rendering it to be undesirable at high Hall parameters exceeded unity; we discuss here the operation of an alternative type, which is the linear Hall MHD channel.

Unlike the continuous-electrode Faraday MHD channel, where a high Hall parameter (β) beyond unity renders that type undesirable; the linear Hall channel actually is designed for high values of the Hall parameter (β) (as high as 10 [172]), and it becomes undesirable at low values of (β).

Figure 3 illustrates the configuration of the linear Hall channel. Instead of separating the electrodes (anode and cathode) vertically, as was the case in the continuous-electrode Faraday channel; they are here separated axially. The positive cathode is at the rear of the channel, while the negative (or reference grounded) anode is at the front of the channel. Multiple vertical short-circuit links are inserted. Each vertical link is an equipotential line, and the electric potential increases downstream toward the cathode. We added some numerical example values, from 0 V at the anode to 30 V at the cathode (these are for explaining the variation of the electric potential, but they are not realistic values due to being very small) [173].

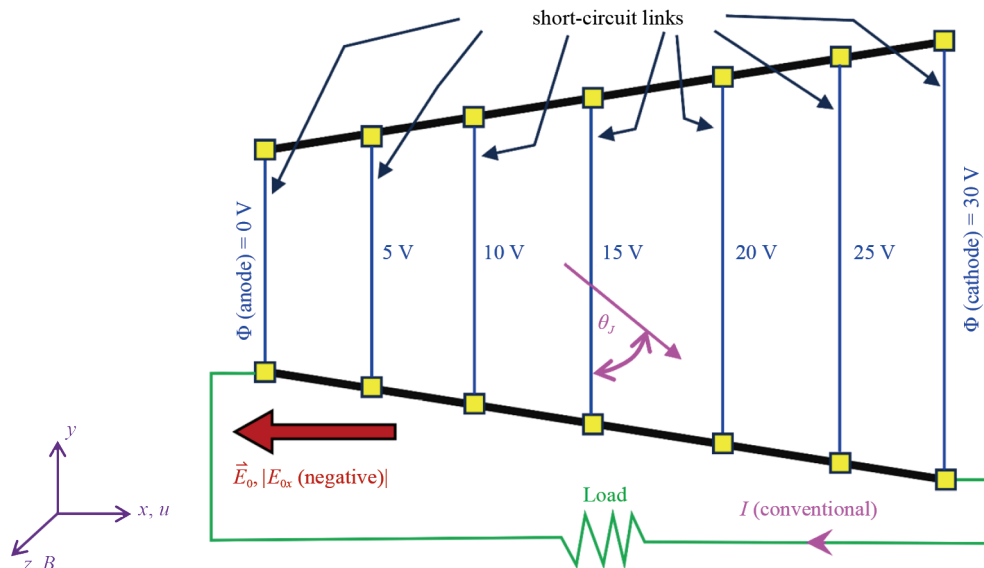


Figure 3. Graphical illustration of a linear Hall channel, with a demonstration of the direction of the current density and the load electric field

It can be seen in the sketch that the load electric field is purely horizontal, pointing upstream in the direction of decreasing electric potential (Φ). The load electric field vector (\vec{E}_0) is the opposite of the gradient of electric potential (Φ). Mathematically, this can be expressed as

$$\vec{E}_0 = -\nabla\Phi \quad (54)$$

Due to the vertical shorting introduced in the linear Hall MHD channel (making the equipotential lines vertical), the load electric field vector (\vec{E}_0) is purely horizontal, in the direction of the negative x -axis. Thus, the vertical component of the load electric field vector (E_{0y}) vanishes in the linear Hall channel. Therefore,

$$E_{0y} = 0 \quad (55)$$

$$\vec{E}_0 = E_{0x} \hat{i} = -|E_{0x}| \hat{i} \quad (56)$$

$$\theta_\Phi = \tan^{-1} \left(\frac{E_{0y}}{|E_{0x}|} \right) = \tan^{-1} \left(\frac{0}{|E_{0x}|} \right) = 0^\circ \quad (57)$$

Recognizing that (E_{0x}) has a negative value ($E_{0x} = -|E_{0x}|$), then from Equation (38), we can write

$$E_{0x} = -K_H \beta u B \quad (58)$$

Using the above equation and Equation (55) in Equation (29) and also in Equation (30), gives a customized form for the electric current-density components suitable for linear Hall channels as

$$J_x = \frac{\sigma}{1+\beta^2} (-K_H \beta u B + \beta u B) = \frac{\sigma}{1+\beta^2} \beta u B (1 - K_H) \quad (59)$$

$$J_y = \frac{\sigma}{1+\beta^2} (-u B - \beta^2 K_H u B) = -\frac{\sigma}{1+\beta^2} u B (1 + \beta^2 K_H) \quad (60)$$

The above two equations show that the current density vector in linear Hall channels has a positive x -component ($J_x = |J_x|$) but a negative y -component ($J_y = -|J_y|$). This is illustrated in the previous sketch, with the tilt angle (acute angle, measured from the y -axis) of the current-density vector (θ_J) when measured from the vertical is mathematically expressed as

$$\theta_J = \tan^{-1} \left(\frac{J_x}{|J_y|} \right) = \tan^{-1} \left(\frac{\beta (1 - K_H)}{1 + \beta^2 K_H} \right) \quad (61)$$

In order for the current density vector (\vec{J}) to be parallel, the Hall parameter (β) has to be uniform, and this implies uniformity in the plasma thermo-chemical properties (chemical composition, temperature, and pressure).

From Equation (39), the Direct Current (DC) electric power delivered to the load per unit volume of plasma in the case of the linear Hall channel (P_H) is

$$P_H : K_H \beta u B J_x = K_H \beta u B \frac{\sigma}{1+\beta^2} \beta u B (1-K_H) = \frac{\sigma}{1+\beta^2} u^2 B^2 \beta^2 K_H (1-K_H) \quad (62)$$

Similar to the case of continuous-electrode Faraday channels, when the above expression is optimized with respect to the Hall load factor (K_H), the optimum case occurs at ($K_H = 0.5$). This means that the external resistance of the matched (optimized) load is equal to the internal resistance of the MHD generator, or

$$R_{L, \text{opt-H}} = R_G \quad (63)$$

In such a case of ($K_H = 0.5$), the matched-load optimized power dissipation to the load (per unit plasma volume) in the linear Hall channel is

$$P_{H, \text{opt}} = 0.25 \frac{\beta^2}{1+\beta^2} \sigma u^2 B^2 \quad (64)$$

Comparing this expression for ($P_{H, \text{opt}}$) to the one derived earlier for ($P_{F, \text{opt}}$) shows that the power penalty factor $\left(\frac{1}{(1+\beta^2)}\right)$ in the continuous-electrode Faraday becomes $\left(\frac{\beta^2}{(1+\beta^2)}\right)$ in the linear Hall channel. This Hall power penalty factor approaches unity (thus, the penalty diminishes) at high values of the Hall parameter ($\beta \gg 1$). This explains how the linear Hall channel is favored over the continuous-electrode Faraday for high (β). On the other hand, the continuous-electrode Faraday channel exhibits a smaller power penalty at ($\beta < 1$). The power penalty factors for both channel types become equal to 50% at ($\beta = 1$). The ratio of the matched-load volumetric power density for the linear Hall channel compared to the continuous-electrode Faraday channel is the square of the Hall parameter. Therefore,

$$\frac{P_{H, \text{opt}}}{P_{F, \text{opt-cont}}} = \beta^2 \quad (65)$$

To help quantify the advantage of continuous-electrode Faraday MHD generators at low (β), and the advantage of linear Hall MHD generators at high (β), we compare in Table 1 the power penalty factors for both types of MHD linear channels (continuous-electrode and Hall) for a wide range of (β) from 0 to 10. It is apparent that at ($\beta = 2$), the linear Hall channel is four times more useful than the continuous-electrode Faraday channel.

Table 1. Gain in the power output for the linear Hall channel compared to the continuous-electrode Faraday channel at different Hall parameters

Hall parameter	Power penalty factor		
	Continuous-electrode Faraday	Linear Hall	$\frac{P_{H, \text{opt}}}{P_{F, \text{opt-cont}}} = \beta^2$
0	100%	0%	0
0.25	94.1176%	0.0588	0.0625
0.5	80%	20%	0.25
0.75	64%	36%	0.5625
1	50%	50%	1
1.25	39.0244%	60.9756%	1.5625
1.5	30.7692%	69.2308%	2.25
1.75	24.6154%	75.3846%	3.0625
2	20%	80%	4
2.5	13.793%	86.2069%	6.25
3	10%	90%	9
4	5.8824%	94.1176%	16
5	3.8462%	96.1538%	25
6	2.7027%	97.2973%	36
7	2%	98%	49
8	1.5385%	98.4615%	64
9	1.2195%	98.7805%	81
10	0.9901%	99.0099%	100

We point out here that in the linear Hall channel, because there are multiple electric connections (the shorting links) between the anode and cathode pairs, and each of these intermediate electric connections has an electric potential exceeding that of the anode; each of these intermediate links can be used as an intermediate cathode that powers a separate electric load (connected from the other terminal to the global anode at the entrance of the MHD channel). This possibility is illustrated in Figure 4. However, in the current study, we assume in the analysis the simple case of a single electric load connected between the MHD overall anode and overall cathode. This allows consistency when comparing this channel type with the continuous-electrode Faraday channel (which admits only a single electric load).

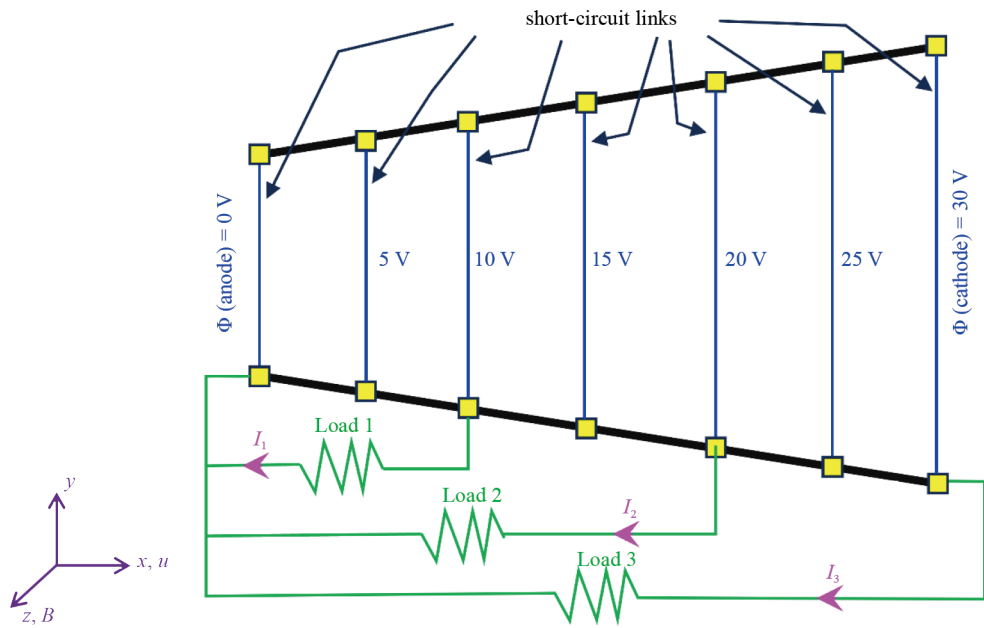


Figure 4. Graphical illustration of a linear Hall channel, in the case of three external loads being powered simultaneously

We conclude this subsection by deriving a special expression for the electric efficiency of the linear Hall channel. From the general expression in Equation (4), a reduced version can be obtained if the channel has uniform electromagnetic properties, and this reduced form is

$$\eta_{\text{elec}, H} = \frac{|J_x E_{0x}| + |J_y E_{0y}|}{u |J_y| B} = \frac{J_x |E_{0x}|}{u |J_y| B} = \frac{\frac{\sigma}{1+\beta^2} \beta u B (1-K_H) K_H \beta u B}{u \frac{\sigma}{1+\beta^2} u B (1+\beta^2 K_H) B} \quad (66)$$

This can be simplified to

$$\eta_{\text{elec}, H} = \frac{\beta^2 (1-K_H) K_H}{1+\beta^2 K_H} = \frac{\beta^2}{1+\beta^2 K_H} (1-K_H) K_H \quad (67)$$

At high Hall parameters ($\beta \rightarrow \infty$), the above expression approaches the following limit:

$$\eta_{\text{elec}, H}(\beta \rightarrow \infty) = 1 - K_H \quad (68)$$

At the optimum Hall load factor ($K_H = 0.5$), the electric efficiency expression in Equation (67) can be further simplified to

$$\eta_{\text{elec}, H}(K_H = 0.5) = 0.25 \frac{\beta^2}{1+0.5 \beta^2} = \frac{\beta^2}{4+2 \beta^2} \quad (69)$$

which we denote as $(\eta_{\text{elec}, H, \text{opt}})$, which refers to the optimality condition of the Hall load factor.

At high Hall parameters ($\beta \rightarrow \infty$), the above expression approaches the following limit:

$$\eta_{\text{elec}, H} (K_H = 0.5, \beta \rightarrow \infty) = \frac{1}{2} \text{ or } 50\% \quad (70)$$

3.4 Segmented-electrode Faraday channel

After discussing the operational conditions and performance of the continuous-electrode Faraday MHD channel and the linear Hall MHD channel, we here discuss a third configuration of MHD generator channels, which is the segmented-electrode Faraday channel.

In Figure 5, we provide a graphical illustration of the segmented-electrode Faraday channel, which clearly differs from both the continuous-electrode Faraday channel and the linear Hall channel. Like the continuous-electrode Faraday channel, the electrodes are separated vertically (along the y -axis); but unlike the continuous-electrode Faraday channel, each electrode (the bottom positive cathode and the top negative anode) is now divided into multiple electrode segments that are electrically insulated from the adjacent segments.

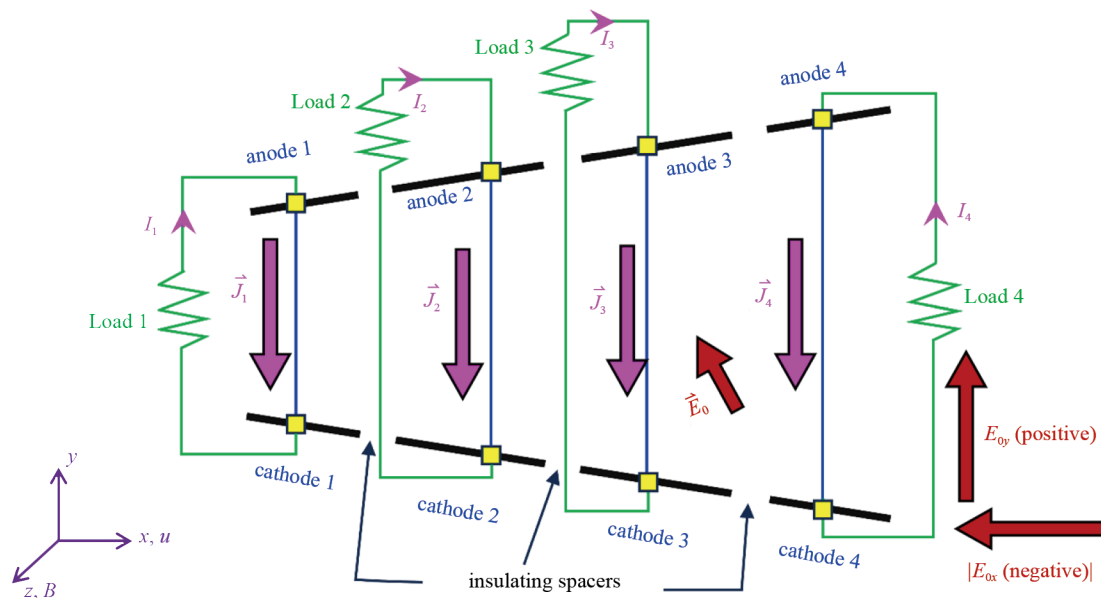


Figure 5. Graphical illustration of a segmented-electrode Faraday channel, with a demonstration of the direction of the current density and the load electric field

The motivation behind the segmented-electrode Faraday channel can be clarified by recalling the adverse effect of the Hall current density (J_x) in the continuous-electrode Faraday channel due to the Hall effect, which causes power loss for the continuous-electrode Faraday channel, in the form of a penalty factor $\left(\frac{1}{(1 + \beta^2)}\right)$. Operating under a condition of vanishing Hall parameter ($\beta = 0$) eliminates this penalty because the penalty factor becomes unity. However, such a condition of zero Hall parameter also means zero electric conductivity, as implied by Equation (6) and Equation (7).

Therefore, an alternative method of avoiding the power loss under non-zero Hall parameter is to adapt the electric connectivity such that the Hall current density (J_x) vanishes, even with the presence of the unavoidable Hall effect.

In order to suppress the Hall current density, the top and bottom electrodes are segmented into multiple segments, and this arrangement does not give a chance for the Hall current density to develop. Ideally, there should be an infinite

number of segments. However, a finite number of segments is practically possible. This resembles the lamination of a solid iron core in an electric transformer in order to suppress the undesirable but unavoidable eddy currents [174–176].

For each pair of opposite segments (cathode and anode), an external load is connected. This might be a drawback in this channel configuration, where having multiple individual loads may not represent the exact demand pattern.

When assuming that the Hall current density successfully vanishes, the following condition becomes a characteristic feature of the segmented-electrode Faraday channel:

$$J_x = 0 \quad (71)$$

Consequently, this means that the inclination angles of the electric current-density vectors (\vec{J}), measured from the vertical are zero. Therefore, each electric current-density vector (\vec{J}) is perfectly vertical (pointing down, from the top anode segment to the bottom cathode segment). Mathematically, this is expressed as

$$\theta_J = \tan^{-1} \left(\frac{J_x}{|J_y|} \right) = \tan^{-1} \left(\frac{0}{|J_y|} \right) = 0^\circ \quad (72)$$

Therefore, in the segmented-electrode Faraday channel; the direction of the current density vectors is restricted to the vertical orientation. However, the load electric field vectors are not subject to such a constraint. In fact, the load electric field possesses an axial component (E_{0x}) and a vertical component (E_{0y}). Like the continuous-electrode Faraday channel, Equation (33) for (E_{0y}) is still valid.

This means that (E_{0y}) is positive (pointing upward toward the negative anodes).

However, the axial component of the load electric field vector (E_{0x}) is no longer zero in the segmented-electrode Faraday channel as was the case in the continuous-electrode Faraday channel. The expression for (E_{0x}) can be derived from its general expression in Equation (40). After setting ($J_x = 0$) in Equation (40), we obtain a condition on (E_{0x}) as

$$0 = \frac{\sigma}{1 + \beta^2} (E_{0x} + \beta u B [1 - K_F]) \quad (73)$$

This leads to the following expression for (E_{0x}) in the case of a segmented-electrode Faraday channel:

$$E_{0x} = -\beta u B (1 - K_F) \quad (74)$$

This shows that (E_{0x}) is negative, which in turn means that the electric potential (Φ) decreases in the axial direction, as the x -coordinate increases.

The absolute value of the local acute inclination angle (θ_Φ) of the equipotential lines (measured from the “vertical” y -axis) in the segmented-electrode Faraday channel can be described as

$$\theta_\Phi = \tan^{-1} \left(\frac{E_{0y}}{|E_{0x}|} \right) = \tan^{-1} \left(\frac{K_F u B}{\beta u B (1 - K_F)} \right) = \tan^{-1} \left(\frac{K_F}{\beta (1 - K_F)} \right) \quad (75)$$

Due to the dependence on the Hall parameter (β), the angle (θ_Φ) is not necessarily constant throughout the MHD channel, and thus the equipotential lines are not necessarily parallel. However, we illustrate them in Figure 6 in the special

case where these equipotential lines are parallel straight lines (for simplicity), and we also show in this figure how the angle (θ_Φ) is defined.

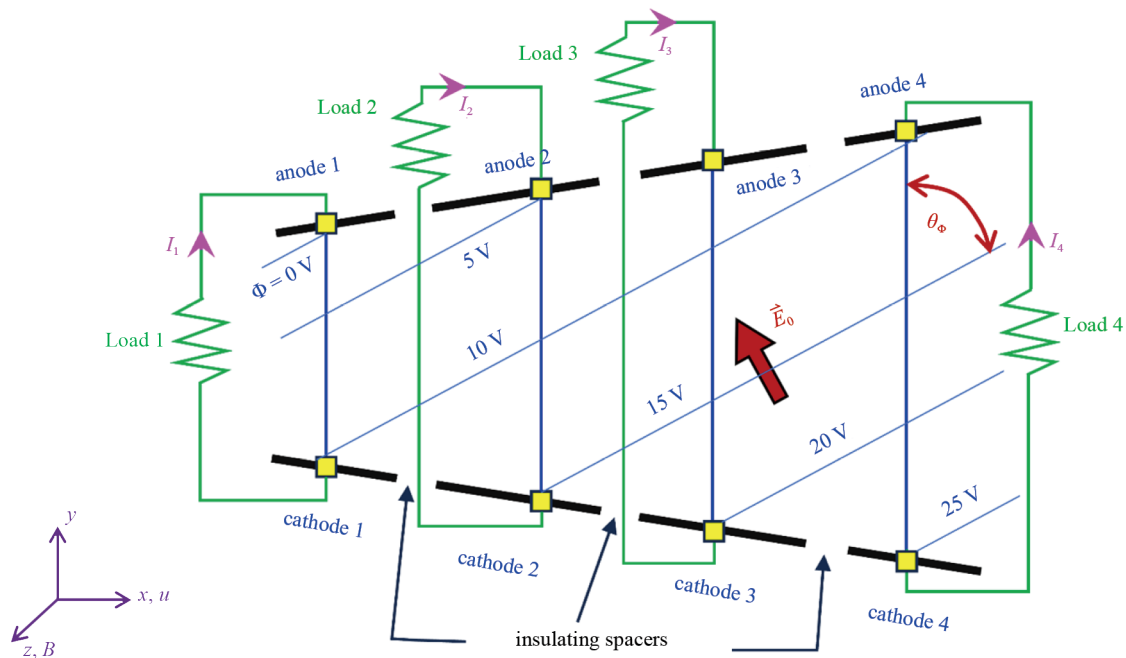


Figure 6. Graphical illustration of a segmented-electrode Faraday channel, with a demonstration of the direction of the current density and the load electric field

From Equation (41), the y -component of the current density in the segmented-electrode Faraday channel is obtained by using Equation (74), which gives:

$$J_y = \frac{\sigma}{1 + \beta^2} (-\beta^2 u B [1 - K_F] - u B [1 - K_F]) = -\frac{\sigma}{1 + \beta^2} u B (1 - K_F) (1 + \beta^2) \quad (76)$$

Thus,

$$J_y = -\sigma u B (1 - K_F) \quad (77)$$

This shows that the electric current-density is downward (having a negative sign).

From Equation (35), the Direct Current (DC) electric power delivered to the load (treating the multiple connected loads as a single one) in the case of the segmented-electrode Faraday channel per unit volume of plasma (P_{F-seg}) is:

$$P_{F-seg} = K_F u B |J_y| = K_F u B \sigma u B (1 - K_F) = \sigma u^2 B^2 K_F (1 - K_F) \quad (78)$$

By comparing this expression for (P_{F-seg}) to the counterpart expression of (P_{F-cont}) in the case of the continuous-electrode Faraday channel in Equation (49), it is evident that the penalty factor of $\left(\frac{1}{(1 + \beta^2)}\right)$ does not appear in the case

of the segmented-electrode Faraday channel. Thus, the electrode segmentation in the Faraday-type channel is successful in making the channel performance independent of the Hall effect, but multiple electrode pairs and loads replace the simpler configuration of a single electrode pair and single load in the case of the continuous-electrode Faraday channel.

As in the case of the continuous-electrode Faraday channel, the optimized output Direct Current (DC) power to the load occurs at a matched load with ($K_F = 0.5$) or ($R_{L, \text{opt-F}} = R_G$). The optimized (matched-load) volumetric power density in the case of the segmented-electrode Faraday channel is:

$$P_{F-\text{seg, opt}} = 0.25\sigma u^2 B^2 \quad (79)$$

This is the same as the ideal (at the theoretical limit of vanishing Hall parameter) volumetric power density for the continuous-electrode Faraday channel with optimized (matched) load in Equation (52).

Comparing this expression for ($P_{F-\text{seg, opt}}$) to the expression of ($P_{H, \text{opt}}$) in the case of the linear Hall channel in Equation (64), it becomes clear that the penalty factor of $\left(\frac{\beta^2}{(1+\beta^2)}\right)$ no longer appears for the case of the segmented-electrode Faraday channel.

We conclude this subsection by deriving a special expression for the electric efficiency of the segmented-electrode Faraday channel. From the general expression in Equation (4), a reduced version can be obtained if the channel has uniform electromagnetic properties, and this reduced form is:

$$\eta_{\text{elec, F-seg}} = \frac{|J_x E_{0x}| + |J_y E_{0y}|}{u|J_y|B} = \frac{|J_y|E_{0y}}{u|J_y|B} = \frac{E_{0y}}{uB} = \frac{K_F uB}{uB} = K_F \quad (80)$$

Thus, the electric efficiency reduces to the Faraday load factor (K_F) in the case of a segmented-electrode Faraday channel with uniform properties. This is the same result obtained for the continuous-electrode Faraday channel. This also means that the optimum electric efficiency ($\eta_{\text{elec, F-seg, opt}}$) in this channel configuration is 0.5 or 50%.

3.5 Diagonal-electrode channel

In the previous subsection, we showed how the segmented-electrode Faraday Magnetohydrodynamic (MHD) channel possesses desirable performance through ideal utilization of the MHD volume without being affected by the Hall parameter. However, we showed that this ideal condition comes at the expense of complicating the construction and electric connectivity, while a large number (theoretically infinite number) of anode-cathode pairs are needed for powering a large number of individual loads.

It is desirable to design a fourth configuration of linear MHD channels that maintains the excellent performance of the segmented-electrode Faraday channel while being less demanding in terms of the construction complexity and being able to power a single load if wanted. We here discuss this design, referred to as the (diagonal-electrode channel) or the (diagonal channel).

In the diagonal-electrode MHD channel, the suppression of the Hall current is achieved, but not through complicated segmentation as in the case of the segmented-electrode Faraday channel. Rather, this condition of ($J_x = 0$) attained through manipulating the direction of the electric field vectors such that their direction is the same as those implied in the segmented-electrode Faraday channel. This also means that the inclination angle of the equipotential lines (measured from the vertical) should also match the one found in the segmented-electrode Faraday channel.

It is useful to repeat Equations (75) here the mathematical expression arrived at in the previous subsection for the absolute value of the local acute inclination angle (θ_Φ) of the equipotential line (measured from the “vertical” y-axis) in the segmented-electrode Faraday channel.

This means that the tangent of the equipotential inclination is:

$$\tan(\theta_\Phi) = \frac{K_F}{\beta(1 - K_F)} \quad (81)$$

The above expression can be manipulated to derive a mathematical expression for the Faraday load factor (K_F) as a function of the equipotential lines angle (θ_Φ). The result is:

$$K_F = \frac{\beta \tan(\theta_\Phi)}{1 + \beta \tan(\theta_\Phi)} \quad (82)$$

The control of the direction of the equipotential lines in the diagonal channel is achieved by introducing inclined short-circuit links, tilted at the desired inclination angle (θ_Φ) from the vertical as shown in Figure 7. In this sketch, we assume a variation of the electric potential from 0 V at the MHD anode (located at the entrance of the MHD channel) to 20 V at the MHD cathode (located at the rear of the MHD channel). We also assume a single external load connected between these two primary electrodes (the primary anode and the primary cathode).

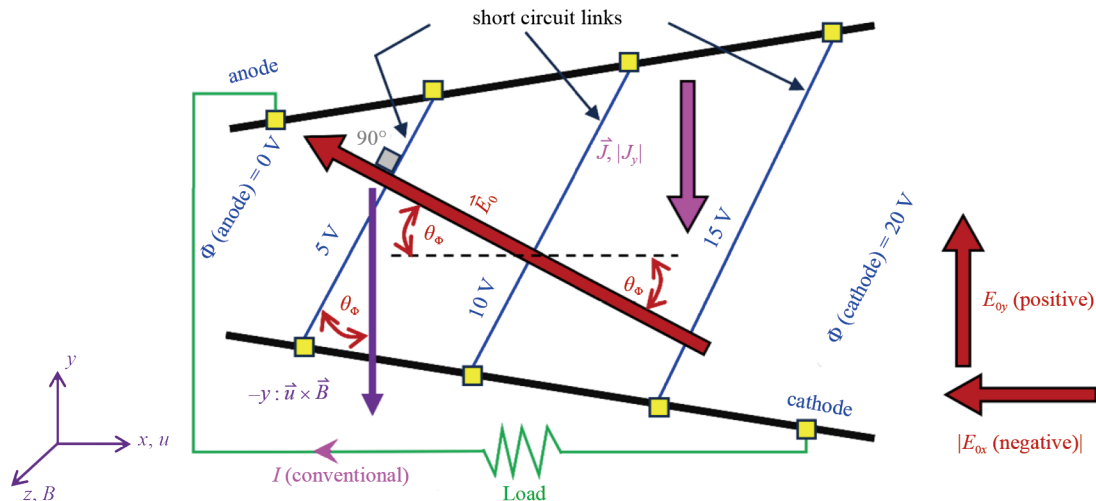


Figure 7. Graphical illustration of a diagonal-electrode channel, with a demonstration of the direction of the current density and the load electric field

From Equation (75), we can also extract a geometric condition of the load electric field vector (\vec{E}_0), whose negative axial component (E_{0x}) and its positive vertical component (E_{0y}) should be related according through the angle (θ_Φ) as:

$$E_{0x} = -\frac{E_{0y}}{\tan(\theta_\Phi)} = -E_{0y} \cot(\theta_\Phi) \quad (83)$$

As in the Faraday-type channels, it's given as Equation (33).

Therefore, in the diagonal MHD channel, the (negative) axial component of the load electric field can be expressed using Equation (83) and Equation (33) as:

$$E_{0x} = -\frac{K_F u B}{\tan(\theta_\Phi)} = -K_F u B \cot(\theta_\Phi) \quad (84)$$

Using the expression of (E_{0x}) in Equation (84) and the expression of $(\tan(\theta_\Phi))$ in Equation (81) gives another form for expressing the axial component (E_{0x}) , which is:

$$E_{0x} = -\frac{K_F u B}{\frac{K_F}{\beta(1-K_F)}} = -u B \beta (1 - K_F) \quad (85)$$

It is useful now to repeat the general expression of the axial component (J_x) of the electric current-density vector (\vec{J}) for Faraday-type channels (Equation (40)).

Using the expression for the target profile of (E_{0x}) for a diagonal channel, as provided through Equation (85), in the above equation for (J_x) shows that the component (J_x) automatically vanishes, as follows:

$$J_x = \frac{\sigma}{1+\beta^2} (-u B \beta [1 - K_F] + u B \beta [1 - K_F]) = \frac{\sigma}{1+\beta^2} u B \beta (0) = 0 \quad (86)$$

The vanishing of the axial component of the electric current-density vectors (\vec{J}) means that these vectors are exactly vertical (parallel to the y-axis). Consequently, the inclination angles of these vectors (θ_J) , measured from the vertical, are zero. This situation is identical to the one obtained in the segmented-electrode Faraday channel (Equation (72)).

We also repeat the general expression of the vertical component (J_y) of the electric current-density vector (\vec{J}) for Faraday-type channels (Equation (41)).

Using the earlier expression for (E_{0x}) , as given in Equation (85), shows that for the diagonal channel, the component (J_y) becomes:

$$J_y = \frac{\sigma}{1+\beta^2} (-u B \beta^2 [1 - K_F] - u B [1 - K_F]) = -\frac{\sigma}{1+\beta^2} u B [1 - K_F] (1 + \beta^2) \quad (87)$$

Thus, for the diagonal channel, we have the same expression for (J_y) as the one reached earlier for the segmented-electrode Faraday channel (Equation (77)).

The Direct Current (DC) electric power delivered to the load (treating the multiple connected loads as a single one) in the case of the diagonal-electrode channel per unit volume of plasma (P_D) is the same as the one provided earlier for the segmented-electrode Faraday channel (P_{F-seg}) . The mathematical expression for (P_D) is:

$$P_D = K_F u B |J_y| = K_F u B \sigma u B (1 - K_F) = \sigma u^2 B^2 K_F (1 - K_F) \quad (88)$$

Therefore, neither the penalty factor $\left(\frac{1}{(1+\beta^2)}\right)$ nor the penalty factor $\left(\frac{\beta^2}{(1+\beta^2)}\right)$ appear in the present case of a diagonal-electrode channel.

As in the case of the continuous-electrode Faraday channel and the segmented-electrode Faraday channel, the optimized value of (K_F) is 0.5; and optimized power density in the case of the diagonal-electrode channel is:

$$P_{D, \text{opt}} = 0.25 \sigma u^2 B^2 \quad (89)$$

We would like to add three remarks about the diagonal MHD channel.

The first remark is that, despite the attractive performance of the diagonal channel as described above, it should be noted that this is constrained to a particular value of (K_F) and a corresponding uniform value of (β). In reality, it is difficult to maintain such a specific operating point (on-design operation), and thus operating at off-design regimes is likely to happen [177–179]. In the off-design condition, the expressions we provided for the diagonal channel break, as these assume a perfect design point.

The second remark is that the diagonal-electrode channel reduces to a linear Hall channel in the special value of ($\theta_\Phi = 0^\circ$), which corresponds to vertical shorting links.

The third remark is that, as was the case for the linear Hall channel, the diagonal-electrode channel permits powering multiple loads simultaneously because there are multiple electric connections (the shorting links) that offer multiple levels of electric potential. This possibility is illustrated in Figure 8.

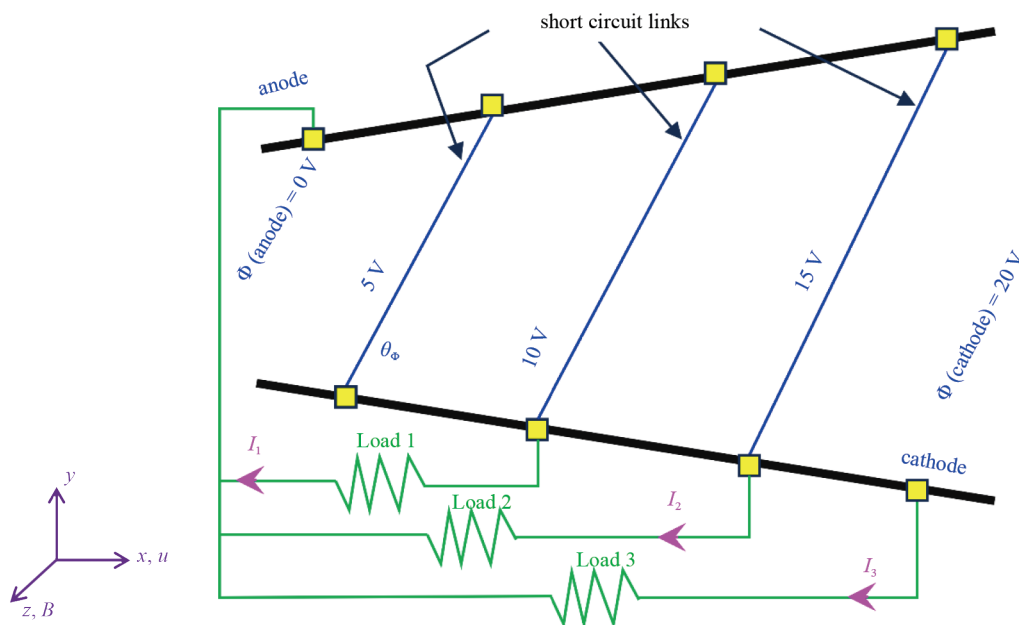


Figure 8. Graphical illustration of a diagonal-electrode channel, in the case of three external loads being powered simultaneously

As done for the previous three subsections, we conclude this subsection by deriving a special expression for the electric efficiency of the diagonal-electrode channel. From the general expression in Equation (4), a reduced version can be obtained if the channel has uniform electromagnetic properties and it is operating at its design point, and this reduced form is:

$$\eta_{\text{elec}, D} = \frac{|J_x E_{0x}| + |J_y E_{0y}|}{u |J_y| B} = \frac{|J_y| E_{0y}}{u |J_y| B} = \frac{E_{0y}}{u B} = \frac{K_F u B}{u B} = K_F \quad (90)$$

Thus, the electric efficiency is reduced to (K_F) . This is the same result obtained for either the continuous-electrode Faraday channel or the segmented-electrode Faraday channel. This also means that the optimum electric efficiency $(\eta_{\text{elec}, D, \text{opt}})$ in this channel configuration is 0.5 or 50%.

4. Discussion

The purpose of the current section is to augment the presented results by adding two supplementary topics. The first topic is a summary of key equations describing various performance variables for each linear MHD channel type, as derived in detail in the previous section. The second topic is a numerical set of values for some of these key parameters, which is useful for bridging the gap between the preceding theoretical analysis and real applications.

4.1 Summary of MHD channel performance expressions

In this subsection, we compare in Table 2 various key characteristics of the continuous-electrode Faraday channel and the linear Hall channel, whose geometric and electric connectivity are very different.

Table 2. Comparison between two types of linear magnetohydrodynamic channels

Quantity	Continuous-electrode Faraday	Linear Hall
E_{0x}	0	$-K_H \beta u B$
E_{0y}	$K_F u B$	0
θ_Φ	90°	0°
J_x	$\frac{\sigma}{1+\beta^2} \beta u B (1-K_F)$	$\frac{\sigma}{1+\beta^2} \beta u B (1-K_H)$
J_y	$-\frac{\sigma}{1+\beta^2} u B (1-K_F)$	$-\frac{\sigma}{1+\beta^2} u B (1+\beta^2 K_H)$
θ_J	$\tan^{-1}(\beta)$	$\tan^{-1}\left(\frac{\beta(1-K_H)}{1+\beta^2 K_H}\right)$
P	$\frac{\sigma}{1+\beta^2} u^2 B^2 K_F (1-K_F)$	$\frac{\sigma}{1+\beta^2} u^2 B^2 \beta^2 K_H (1-K_H)$
P_{opt}	$0.25 \frac{1}{1+\beta^2} \sigma u^2 B^2$	$0.25 \frac{\beta^2}{1+\beta^2} \sigma u^2 B^2$
η_{elec}	K_F	$\frac{\beta^2(1-K_H)K_H}{1+\beta^2 K_H}$
Number of loads	1	1 or more

Then in Table 3, we provide a similar comparison, but between the segmented-electrode Faraday channel and its performance-equivalent diagonal-electrode channel (when operating at its design point). It can be seen that these two types are very similar in terms of their operation.

Table 3. Comparison between the other two types of linear magnetohydrodynamic channels

Quantity	Segmented-electrode Faraday	Diagonal-electrode
E_{0x}	$-\beta uB(1 - K_F)$	Same as segmented-electrode Faraday
E_{0y}	$K_F uB$	Same as segmented-electrode Faraday
θ_Φ	$\tan^{-1} \left(\frac{K_F}{\beta(1 - K_F)} \right)$	Same as segmented-electrode Faraday
J_x	0	Same as segmented-electrode Faraday
J_y	$-\sigma uB(1 - K_F)$	Same as segmented-electrode Faraday
θ_J	0°	Same as segmented-electrode Faraday
P	$\sigma u^2 B^2 K_F(1 - K_F)$	Same as segmented-electrode Faraday
P_{opt}	$0.25 \sigma u^2 B^2$	Same as segmented-electrode Faraday
η_{elec}	K_F	Same as segmented-electrode Faraday
Number of loads	multiple	1 or more

4.2 Numerical examples of linear MHD channel performance quantities

In the current subsection, we provide a quantitative estimate of some performance quantities presented above, based on typical values that can be encountered in real applications. This is summarized in Table 4.

Table 4. Magnitudes of important physical quantities in linear MHD channels at selected representative conditions

Quantity	Magnitude	Reference
σ	5 S/m	[180–185]
u	2,000 m/s	[186–188]
B	5 T	[189–194]
$\beta(F\text{-cont})$	1	[195, 196]
$K_F(F\text{-cont})$	0.5	The current study itself
$E_{0y}(F\text{-cont})$	5,000 V/m (5 kV/m)	The current study itself
$ J_y(F\text{-cont}) $	12,500 A/m ² (12.5 kA/m ²)	The current study itself
$P_{F\text{-cont, opt}}$	62,500,000 W/m ³ (62.5 MW/m ³)	The current study itself
$\eta_{\text{elec}, F\text{-cont, opt}}$	50%	The current study itself
$\beta(\text{Hall})$	5	[197–200]
$K_H(\text{Hall})$	0.5	The current study itself
$ E_{0x}(\text{Hall}) $	25,000 V/m (25 kV/m)	The current study itself
$J_x(\text{Hall})$	4,807.6923 A/m ² (4.808 kA/m ²)	The current study itself
$P_{H, \text{opt}}$	120,192,300 W/m ³ (120.19 MW/m ³)	The current study itself
$\eta_{\text{elec}, H, \text{opt}}$	46.30%	The current study itself
$K_F(F\text{-seg})$	0.5	The current study itself
$E_{0y}(F\text{-seg})$	5,000 V/m (5 kV/m)	The current study itself
$ J_y(F\text{-seg}) $	25,000 A/m ² (25 kA/m ²)	The current study itself
$P_{F\text{-seg, opt}}$	125,000,000 W/m ³ (125 MW/m ³)	The current study itself
$\eta_{\text{elec}, F\text{-seg, opt}}$	50%	The current study itself
$P_{D, \text{opt}}$	125,000,000 W/m ³ (125 MW/m ³)	The current study itself
$\eta_{\text{elec}, D, \text{opt}}$	50%	The current study itself

In relation to recent studies, some of the above numerical estimations appear compatible. For example; atmospheric air-fuel combustion plasma with 0.125% cesium seeding (mole fraction) was found to enable an optimized ideal volumetric power density of 129.51 MW/m³ for benchmarking [201], which is close to the above estimation of 125 MW/m³. In another study; atmospheric air-fuel combustion plasma was shown to allow an optimized ideal volumetric power density of 104.49 MW/m³ with 1% potassium seeding by mole [202], which is also close to the above estimation of 125 MW/m³.

It is useful to add here that our analysis suggests that the volumetric power density depends linearly on the plasma electric conductivity. However, it depends quadratically on the magnetic-field flux density, the plasma speed, or the load factor.

5. Conclusions

In the current study, we provided a detailed mathematical analysis of the four main types of linear Magnetohydrodynamic (MHD) channels for power generation applications. Namely, these are the (1) continuous-electrode Faraday channel, (2) segmented-electrode Faraday channel, (3) linear Hall channel, and (4) diagonal-electrode channel. Through applying some assumptions (unidirectional applied magnetic field, unidirectional plasma velocity, low magnetic Reynolds number, and two-dimensional electric field), closed-form analytical expressions were derived to describe the operation and power generation performance of these four channel types. The study is enriched by contrasting the sets of equations governing various performance variables for each of the four linear MHD channel types, as well as by providing quantitative estimates to demonstrate the possible magnitude of key performance quantities of these four linear MHD channel types.

Data availability statement

The data that support the findings of this study are available within the article itself.

Conflict of interest

The author declares that he has no known competing financial interests or personal relationships that could have appeared to influence the work reported in this paper.

References

- [1] Smil V. *Energy and Civilization: A History*. MIT Press; 2017.
- [2] Marzouk OA. Compilation of smart cities attributes and quantitative identification of mismatch in rankings. *Journal of Engineering*. 2022; 2022: 5981551. Available from: <https://doi.org/10.1155/2022/5981551>.
- [3] Ember. *Global Electricity Review 2024*. London, UK: Ember; 2024. Available from: <https://ember-energy.org/app/uploads/2024/05/Report-Global-Electricity-Review-2024.pdf> [Accessed 16th March 2025].
- [4] International Energy Agency (IEA). *Global Electricity Generation by Source, 2014-2025*. 2024. Available from: <https://www.iea.org/data-and-statistics/charts/global-electricity-generation-by-source-2014-2025> [Accessed 16th March 2025].
- [5] Santiago I, Moreno-Munoz A, Quintero-Jiménez P, Garcia-Torres F, Gonzalez-Redondo MJ. Electricity demand during pandemic times: The case of the COVID-19 in Spain. *Energy Policy*. 2021; 148: 111964. Available from: <https://doi.org/10.1016/j.enpol.2020.111964>.
- [6] Marzouk OA. Adiabatic flame temperatures for Oxy-methane, Oxy-hydrogen, Air-methane, and Air-hydrogen stoichiometric combustion using the NASA CEARUN tool, GRI-Mech 3.0 reaction mechanism, and cantera python package. *Engineering, Technology & Applied Science Research*. 2023; 13: 11437-11444. Available from: <https://doi.org/10.48084/etasr.6132>.

- [7] Xie T, Wang P. Analysis of NO formation in counter-flow premixed hydrogen-air flame. *Transactions of the Canadian Society for Mechanical Engineering*. 2013; 37: 851-859. Available from: <https://doi.org/10.1139/tcsme-2013-0072>.
- [8] Marzouk OA. Subcritical and supercritical Rankine steam cycles, under elevated temperatures up to 900 °C and absolute pressures up to 400 bara. *Advances in Mechanical Engineering*. 2024; 16: 16878132231221065. Available from: <https://doi.org/10.1177/16878132231221065>.
- [9] Demirbas A. Hazardous emissions, global climate change and environmental precautions. *Energy Sources, Part B: Economics, Planning, and Policy*. 2006; 1: 75-84. Available from: <https://doi.org/10.1080/009083190881472>.
- [10] Marzouk OA. Zero carbon ready metrics for a single-family home in the sultanate of oman based on EDGE certification system for green buildings. *Sustainability*. 2023; 15: 13856. Available from: <https://doi.org/10.3390/su151813856>.
- [11] Peyvandi M, Hajinezhad A, Moosavian SF. Investigating the intensity of GHG emissions from electricity production in Iran using renewable sources. *Results in Engineering*. 2023; 17: 100819. Available from: <https://doi.org/10.1016/j.rineng.2022.100819>.
- [12] Marzouk OA. Assessment of global warming in Al Buraimi, Sultanate of Oman based on statistical analysis of NASA POWER data over 39 years, and testing the reliability of NASA POWER against meteorological measurements. *Heliyon*. 2021; 7: e06625. Available from: <https://doi.org/10.1016/j.heliyon.2021.e06625>.
- [13] El Bosaty A, Khafagy S. Reducing greenhouse gas emissions in oil extraction: a case study of solar energy utilization in petroFarah. In: *Mediterranean Offshore Conference*. Alexandria, Egypt: OnePetro; 2024. Available from: <https://doi.org/10.2118/223370-MS>.
- [14] Marzouk OA. Tilt sensitivity for a scalable one-hectare photovoltaic power plant composed of parallel racks in Muscat. *Cogent Engineering*. 2022; 9: 2029243. Available from: <https://doi.org/10.1080/23311916.2022.2029243>.
- [15] Kakran S, Rathore JS, Sidhu A, Kumar A. Solar energy advances and CO₂ emissions: A comparative review of leading nations' path to sustainable future. *Journal of Cleaner Production*. 2024; 475: 143598. Available from: <https://doi.org/10.1016/j.jclepro.2024.143598>.
- [16] Marzouk OA. Lookup tables for power generation performance of photovoltaic systems covering 40 geographic locations (Wilayats) in the sultanate of Oman, with and without solar tracking, and general perspectives about solar irradiation. *Sustainability*. 2021; 13: 13209. Available from: <https://doi.org/10.3390/su132313209>.
- [17] European Wind Energy Association (EWEA). *The Economics of Wind Energy*. Brussels, Belgium: EWEA; 2009.
- [18] Marzouk OA. Energy generation intensity (EGI) of solar updraft tower (SUT) power plants relative to CSP plants and PV power plants using the new energy simulator "Aladdin". *Energies*. 2024; 17: 405. Available from: <https://doi.org/10.3390/en17020405>.
- [19] Joselin Herbert GM, Iniyan S, Sreevalsan E, Rajapandian S. A review of wind energy technologies. *Renewable and Sustainable Energy Reviews*. 2007; 11: 1117-1145. Available from: <https://doi.org/10.1016/j.rser.2005.08.004>.
- [20] Webb J, Longden T, Boulaire F, Gono M, Wilson C. The application of green finance to the production of blue and green hydrogen: A comparative study. *Renewable Energy*. 2023; 219: 119236. Available from: <https://doi.org/10.1016/j.renene.2023.119236>.
- [21] Marzouk OA. Performance analysis of shell-and-tube dehydrogenation module. *International Journal of Energy Research*. 2017; 41: 604-610. Available from: <https://doi.org/10.1002/er.3637>.
- [22] Huang H, Li L, Zhu G, Li L. Performance investigation of plasma magnetohydrodynamic power generator. *Applied Mathematics and Mechanics (English Edition)*. 2018; 39: 423-436. Available from: <https://doi.org/10.1007/s10483-018-2310-9>.
- [23] Marzouk OA. One-way and two-way couplings of CFD and structural models and application to the wake-body interaction. *Applied Mathematical Modelling*. 2011; 35: 1036-1053. Available from: <https://doi.org/10.1016/j.apm.2010.07.049>.
- [24] Shimizu K, Okuno Y, Yamasaki H, Kabashima S. Numerical simulation of plasma and fluid flow in a shock-tube-driven disk MHD generator. *IEEE Transactions on Plasma Science*. 2000; 28: 1706-1712. Available from: <https://doi.org/10.1109/27.901257>.
- [25] Wang S, Liu Z, Huang H, Lu P. Performance investigations of the two-phase mixer for liquid metal magnetohydrodynamic generator. *Theoretical and Computational Fluid Dynamics*. 2025; 39: 18. Available from: <https://doi.org/10.1007/s00162-025-00738-0>.

- [26] Zhao L, Peng A. Review of conductive reciprocating liquid metal magnetohydrodynamic generators. *Energies*. 2025; 18: 959. Available from: <https://doi.org/10.3390/en18040959>.
- [27] Li L, Wang G, Liao Y, Wu Q, Ning P. Study on the influence of hall effect on the performance of disk generation channel. *Magnetochemistry*. 2025; 11: 19. Available from: <https://doi.org/10.3390/magnetochemistry11030019>.
- [28] Noda K, Kawasaki A, Higashino K. An experimental study on magnetohydrodynamic power generation using a rotating detonation combustor. In: *AIAA SCITECH 2025 Forum*. Orlando, Florida, USA: AIAA; 2025. Available from: <https://doi.org/10.2514/6.2025-0203>.
- [29] Marzouk OA. Radiant heat transfer in nitrogen-free combustion environments. *International Journal of Nonlinear Sciences and Numerical Simulation*. 2018; 19: 175-188. Available from: <https://doi.org/10.1515/ijnsns-2017-0106>.
- [30] Masuda R, Matsumoto M, Kawasaki A, Okuno Y. Power generation characteristics of disk-shaped magnetohydrodynamic generator driven by rotating detonation. *Journal of Propulsion and Power*. 2025; 41: 125-134. Available from: <https://doi.org/10.2514/1.B39577>.
- [31] Kayukawa N. Open-cycle magnetohydrodynamic electrical power generation: a review and future perspectives. *Progress in Energy and Combustion Science*. 2004; 30: 33-60. Available from: <https://doi.org/10.1016/j.peccs.2003.08.003>.
- [32] Ork K, Okuno Y. Numerical study on performance of a xenon-seeded neon plasma magnetohydrodynamic electrical power generator. *IEEE Transactions on Plasma Science*. 2024; 52: 2323-2332. Available from: <https://doi.org/10.1109/TPS.2024.3430198>.
- [33] Foest R, Schmidt M, Becker K. Microplasmas, an emerging field of low-temperature plasma science and technology. *International Journal of Mass Spectrometry*. 2006; 248: 87-102. Available from: <https://doi.org/10.1016/j.ijms.2005.11.010>.
- [34] Marzouk OA. Temperature-dependent functions of the electron-neutral momentum transfer collision cross sections of selected combustion plasma species. *Applied Sciences*. 2023; 13: 11282. Available from: <https://doi.org/10.3390/app132011282>.
- [35] Okuno Y, Kabashima S, Yamasaki H, Harada N, Shioda S. Comparative studies of the performance of closed cycle disk MHD generators using argon, helium and an argon-helium mixture. *Energy Conversion and Management*. 1985; 25: 345-353. Available from: [https://doi.org/10.1016/0196-8904\(85\)90053-6](https://doi.org/10.1016/0196-8904(85)90053-6).
- [36] Veeffkind A. Experiments on plasma-physical aspects of closed cycle MHD power generation. *IEEE Transactions on Plasma Science*. 2004; 32: 2197-2209. Available from: <https://doi.org/10.1109/TPS.2004.838126>.
- [37] Royal Society of Chemistry (RSC). *Caesium - Element Information, Properties and Uses: Periodic Table*. 2025. Available from: <https://periodic-table.rsc.org/element/55/caesium> [Accessed 16th March 2025].
- [38] Smith JF. The Cs-Nb (cesium-niobium) system and the Cs-V (cesium-vanadium) system. *Bulletin of Alloy Phase Diagrams*. 1988; 9: 47-50. Available from: <https://doi.org/10.1007/BF02877459>.
- [39] Kennedy GC, Jayaraman A, Newton RC. Fusion curve and polymorphic transitions of cesium at high pressures. *Physical Review*. 1962; 126: 1363-1366. Available from: <https://doi.org/10.1103/PhysRev.126.1363>.
- [40] National Center for Biotechnology Information (NCBI). *PubChem: Compound Summary for CID 5354618, Cesium*. 2025. Available from: <https://pubchem.ncbi.nlm.nih.gov/compound/5354618> [Accessed 16th March 2025].
- [41] Boulos MI, Fauchais PL, Pfender E. Thermodynamic properties of non-equilibrium plasmas. In: Boulos MI, Fauchais PL, Pfender E. (eds.) *Handbook of Thermal Plasmas*. Cham: Springer International Publishing; 2023. p.385-426. Available from: https://doi.org/10.1007/978-3-030-84936-8_9.
- [42] Meher KC, Tiwari N, Ghorui S. Thermodynamic and transport properties of nitrogen plasma under thermal equilibrium and non-equilibrium conditions. *Plasma Chemistry and Plasma Processing*. 2015; 35: 605-637. Available from: <https://doi.org/10.1007/s11090-015-9615-z>.
- [43] Guo H, Zhang XN, Chen J, Li HP, Ostrikov K. Non-equilibrium synergistic effects in atmospheric pressure plasmas. *Scientific Reports*. 2018; 8: 4783. Available from: <https://doi.org/10.1038/s41598-018-22911-8>.
- [44] Starikovskaia S, Lacoste DA, Colonna G. Non-equilibrium plasma for ignition and combustion enhancement. *European Physical Journal D*. 2021; 75: 231. Available from: <https://doi.org/10.1140/epjd/s10053-021-00240-2>.
- [45] Houben JWM. *Loss Mechanisms in an MHD Generator*. Doctoral dissertation. Technische Hogeschool Eindhoven; 1973. Available from: <https://inis.iaea.org/records/kmqbd-fks05> [Accessed 17th March 2025].
- [46] Rosenbaum M. MHD project at observatorio nacional de fisica cosmica de san miguel [MHD project at national observatory of cosmic physics of San Miguel]. In: *Closed-Cycle MHD Specialists Meeting*. Cleveland, Ohio, USA:

- NASA; 1975. p.1-5. Available from: <https://ntrs.nasa.gov/api/citations/19760066328/downloads/19760066328.pdf> [Accessed 17th March 2025].
- [47] Kobayashi H, Okuno Y, Kabashima S. Three-dimensional simulation of nonequilibrium seeded plasma in closed cycle disk MHD generator. *IEEE Transactions on Plasma Science*. 1997; 25: 380-385. Available from: <https://doi.org/10.1109/27.602515>.
 - [48] Suekane T, Maeda T, Okuno Y, Kabashima S. Numerical simulation on MHD flow in disk closed cycle MHD generator. In: *28th Plasmadynamics and Lasers Conference*. Atlanta, Georgia, USA: AIAA; 1997. Available from: <https://doi.org/10.2514/6.1997-2396>.
 - [49] Okuno Y, Yamasaki H, Kabashima S, Shioda S. Unsteady discharge and fluid flow in a closed-cycle disk MHD generator. *Journal of Propulsion and Power*. 1988; 4: 61-67. Available from: <https://doi.org/10.2514/3.23032>.
 - [50] Sakamoto Y, Sasaki R, Fujino T. Relation between total pressure loss in supersonic nozzle and isentropic efficiency of nonequilibrium disk-shaped MHD generator. *Electrical Engineering in Japan*. 2021; 214: e23342. Available from: <https://doi.org/10.1002/eej.23342>.
 - [51] LUMITOS AG. *ChemEurope: MHD generator*. 2025. Available from: https://www.chemeuropa.com/en/encyclopedia/MHD_generator.html [Accessed 17th March 2025].
 - [52] Harada N, Kien LC, Hishikawa M. Basic studies on closed cycle MHD power generation system for space application. In: *35th AIAA Plasmadynamics and Lasers Conference*. Portland, Oregon, USA: AIAA; 2004. Available from: <https://doi.org/10.2514/6.2004-2365>.
 - [53] Sun E, Yao Y, Zhang Q, Chen F, Xu J, Liu Y. Thermodynamic study of semi-closed rankine cycle based on direct combustion of hydrogen fuel. *International Journal of Hydrogen Energy*. 2024; 92: 1463-1475. Available from: <https://doi.org/10.1016/j.ijhydene.2024.10.371>.
 - [54] Marzouk OA. Reduced-Order Modeling (ROM) of a segmented plug-flow reactor (PFR) for hydrogen separation in integrated gasification combined cycles (IGCC). *Processes*. 2025; 13: 1455. Available from: <https://doi.org/10.3390/pr13051455>.
 - [55] Malik A, Zheng Q, Qureshi SR, Zaidi AA, Yaqoob T, Aziz A. Effect of helium xenon as working fluid on centrifugal compressor of power conversion unit of closed Brayton cycle power plant. *International Journal of Hydrogen Energy*. 2021; 46: 7546-7557. Available from: <https://doi.org/10.1016/j.ijhydene.2020.11.255>.
 - [56] Panchenko VP. Preliminary analysis of the “Sakhalin” world largest pulsed MHD generator. In: *33rd Plasmadynamics and Lasers Conference*. Maui, Hawaii, USA: AIAA; 2002. Available from: <https://doi.org/10.2514/6.2002-2147>.
 - [57] Panchenko VP. Preliminary analysis of the “Sakhalin” world largest pulsed MHD generator. In: *4th Workshop on Magnetoplasma Aerodynamics for Aerospace Applications*. Moscow, Russia; 2002. p.322-331.
 - [58] Koczan GM. Proof of equivalence of Carnot principle to II law of thermodynamics and non-equivalence to Clausius I and Kelvin Principles. *Entropy*. 2022; 24: 392. Available from: <https://doi.org/10.3390/e24030392>.
 - [59] Gujrati PD. Carnot theorem revisited: A critical perspective. *Entropy*. 2025; 27: 346. Available from: <https://doi.org/10.3390/e27040346>.
 - [60] Domínguez-Lozoya JC, Domínguez-Lozoya DR, Cuevas S, Ávalos-Zúñiga RA. MHD generation for sustainable development, from thermal to wave energy conversion: Review. *Sustainability*. 2024; 16: 10041. Available from: <https://doi.org/10.3390/su162210041>.
 - [61] Liu F, Zhu A. Thermodynamic analysis of nuclear closed cycle MHD space power system. *Progress in Nuclear Energy*. 2023; 162: 104755. Available from: <https://doi.org/10.1016/j.pnucene.2023.104755>.
 - [62] Huleihil M. Power efficiency characteristics of MHD thermodynamic gas cycle. *Thermal Science and Engineering Progress*. 2019; 11: 204-212. Available from: <https://doi.org/10.1016/j.tsep.2019.04.001>.
 - [63] Gaskell DR, Laughlin DE. *Introduction to the Thermodynamics of Materials*. 7th ed. Boca Raton, Florida, USA: CRC Press; 2024. Available from: <https://doi.org/10.1201/9781003375388>.
 - [64] Harada N. Characteristics of a disk MHD generator with inlet swirl. *Energy Conversion and Management*. 1999; 40: 305-318. Available from: [https://doi.org/10.1016/S0196-8904\(98\)00097-1](https://doi.org/10.1016/S0196-8904(98)00097-1).
 - [65] Nakamura H, Okamura T, Shioda S. Measurements of properties concerning isentropic efficiency in a nonequilibrium MHD disk generator. *IEEE Transactions on Plasma Science*. 1996; 24: 1125-1132. Available from: <https://doi.org/10.1109/27.533121>.

- [66] Ames Aeronautical Laboratory (AML). *Equations, Tables, and Charts for Compressible Flow*. Moffett Field, California, USA: NACA; 1953. Available from: <https://ntrs.nasa.gov/api/citations/19930091059/downloads/19930091059.pdf> [Accessed 17th February 2025].
- [67] Williams DM, Kamenetskiy DS, Spalart PR. On stagnation pressure increases in calorically perfect, ideal gases. *International Journal of Heat and Fluid Flow*. 2016; 58: 40-53. Available from: <https://doi.org/10.1016/j.ijheatfluidflow.2015.12.005>.
- [68] Fedkiw RP, Merriman B, Osher S. High accuracy numerical methods for thermally perfect gas flows with chemistry. *Journal of Computational Physics*. 1997; 132: 175-190. Available from: <https://doi.org/10.1006/jcph.1996.5622>.
- [69] Di Renzo M, Williams CT, Pirozzoli S. Stagnation enthalpy effects on hypersonic turbulent compression corner flow at moderate Reynolds numbers. *Physical Review Fluids*. 2024; 9: 033401. Available from: <https://doi.org/10.1103/PhysRevFluids.9.033401>.
- [70] Kang J, Wang W, Zhu M. A novel liquid fraction iteration methodology for addressing oscillatory issues in the total enthalpy method. *International Journal of Thermal Sciences*. 2025; 208: 109492. Available from: <https://doi.org/10.1016/j.ijthermalsci.2024.109492>.
- [71] Plasseraud M, Mahesh K. Definition of vortex boundary using stagnation pressure. *Physical Review Fluids*. 2024; 9: 114701. Available from: <https://doi.org/10.1103/PhysRevFluids.9.114701>.
- [72] Marzouk OA. Direct numerical simulations of the flow past a cylinder moving with sinusoidal and nonsinusoidal profiles. *Journal of Fluids Engineering*. 2009; 131: 121201. Available from: <https://doi.org/10.1115/1.4000406>.
- [73] Laney CB. *Computational Gasdynamics*. 1st ed. USA: Cambridge University Press; 1998. Available from: <https://doi.org/10.1017/CBO9780511605604>.
- [74] Du H, Liu C. Research on calculation method of variable specific heat performance of wide-speed range aeroengine. In: *American Society of Mechanical Engineers Digital Collection*. ASME; 2024. Available from: <https://doi.org/10.1115/GT2024-122932>.
- [75] Shetty S, Crasta A, Khan SA. Evaluation of stability derivative of a planar wedge for hypersonic flow for a specific heat ratio 1.667. *AIP Conference Proceedings*. 2025; 3278: 020040. Available from: <https://doi.org/10.1063/5.0262108>.
- [76] Gammie CF. Adiabatic index in fluid models of collisionless black hole accretion. *Astrophysical Journal*. 2025; 980: 193. Available from: <https://doi.org/10.3847/1538-4357/adaea3>.
- [77] Murakami T, Okuno Y. Achievement of the highest performance of disk MHD generator: isentropic efficiency of 60% and enthalpy extraction ratio of 30%. In: *34th AIAA Plasmadynamics and Lasers Conference*. Orlando, Florida, USA: AIAA; 2003. Available from: <https://doi.org/10.2514/6.2003-4170>.
- [78] Seikel GR. Coal-fired open-cycle MHD plants. In: Cooper BR, Ellingson WA. (eds.) *The Science and Technology of Coal and Coal Utilization*. Boston, MA: Springer; 1984. p.307-337. Available from: https://doi.org/10.1007/978-1-4684-4580-0_8.
- [79] Hains FD, Yoler YA. Axisymmetric Magnetohydrodynamic channel flow. *Journal of the Aerospace Sciences*. 1962; 29: 143-150. Available from: <https://doi.org/10.2514/8.9353>.
- [80] Marzouk OA. The Sod gasdynamics problem as a tool for benchmarking face flux construction in the finite volume method. *Scientific African*. 2020; 10: e00573. Available from: <https://doi.org/10.1016/j.sciaf.2020.e00573>.
- [81] Xu Z, Amano R. Simulation of supersonic MHD channel flows. In: *45th AIAA Aerospace Sciences Meeting and Exhibit*. Reno, Nevada, USA: AIAA; 2007. Available from: <https://doi.org/10.2514/6.2007-403>.
- [82] Marzouk OA. A two-step computational aeroacoustics method applied to high-speed flows. *Noise Control Engineering Journal*. 2008; 56: 396. Available from: <https://doi.org/10.3397/1.2978229>.
- [83] Harada S, Hoffmann KA, Augustinus J. Numerical solution of the ideal magnetohydrodynamic equations for a supersonic channel flow. *Journal of Thermophysics and Heat Transfer*. 1998; 12: 507-513. Available from: <https://doi.org/10.2514/2.6397>.
- [84] Amano RS, Xu Z, Lee CH. Numerical simulation of supersonic MHD channel flows. In: *American Society of Mechanical Engineers Digital Collection*. ASME; 2009. p.669-676. Available from: <https://doi.org/10.1115/DETC2007-35129>.
- [85] Marzouk OA. Characteristics of the flow-induced vibration and forces With 1- and 2-DOF vibrations and limiting solid-to-fluid density ratios. *Journal of Vibration and Acoustics*. 2010; 132: 041013. Available from: <https://doi.org/10.1115/1.4001503>.

- [86] Marzouk OA, Nayfeh AH. A study of the forces on an oscillating cylinder. In: *ASME 2007 26th International Conference on Offshore Mechanics and Arctic Engineering (OMAE 2007)*. San Diego, California, USA: ASME; 2009. p.741-752. Available from: <https://doi.org/10.1115/OMAE2007-29163>.
- [87] Bobashev S, Erofeev A, Lapushkina T, Zhukov B, Poniaev S, Vasilieva R, et al. Air plasma produced by gas discharge in supersonic MHD channel. In: *44th AIAA Aerospace Sciences Meeting and Exhibit*. Reno, Nevada, USA: AIAA; 2006. Available from: <https://doi.org/10.2514/6.2006-1373>.
- [88] Bobashev SV, Vasil'eva RV, Erofeev AV, Lapushkina TA, Poniaev SA, Van Wie DM. Local effect of electric and magnetic fields on the position of an attached shock in a supersonic diffuser. *Technical Physics*. 2003; 48: 177-184. Available from: <https://doi.org/10.1134/1.1553557>.
- [89] Lax PA, Elliott S, Gordeyev S, Kemnetz MR, Leonov SB. Flow structure behind spanwise pin array in supersonic flow. *Aerospace*. 2024; 11: 93. Available from: <https://doi.org/10.3390/aerospace11010093>.
- [90] Litchford R, Thompson B, Lineberry J. Pulse detonation MHD experiments. In: *29th AIAA, Plasmadynamics and Lasers Conference*. Albuquerque, New Mexico, USA: AIAA; 1998. Available from: <https://doi.org/10.2514/6.1998-2918>.
- [91] Murray R, Vasilyak L, Carraro M, Zaidi S, Shneider M, Macheret S, et al. Observation of MHD effects with non-equilibrium ionization in cold supersonic air flows. In: *42nd AIAA Aerospace Sciences Meeting and Exhibit*. Reno, Nevada, USA: AIAA; 2004. Available from: <https://doi.org/10.2514/6.2004-1025>.
- [92] Mittal ML, Sarma PRL. Current distribution at the end regions of a magnetohydrodynamic channel. *Journal of Energy*. 1979; 3: 181-183. Available from: <https://doi.org/10.2514/3.47997>.
- [93] Macheret S, Schneider M, Murray R, Zaidi S, Vasilyak L, Miles R. RDHWT/MARIAH II MHD modeling and experiments review. In: *24th AIAA Aerodynamic Measurement Technology and Ground Testing Conference*. Portland, Oregon, USA: AIAA; 2004. Available from: <https://doi.org/10.2514/6.2004-2485>.
- [94] Brogan T. The mark V 32 MW self excited MHD generator. In: *43rd AIAA Plasmadynamics and Lasers Conference*. New Orleans, Louisiana, USA: AIAA; 2012. Available from: <https://doi.org/10.2514/6.2012-3175>.
- [95] Tempelmeyer KE, Rittenhouse LE, Wilson DR. Experiments on a Faraday-type MHD accelerator with series-connected electrodes. *AIAA Journal*. 1965; 3: 2160-2162. Available from: <https://doi.org/10.2514/3.3335>.
- [96] Litchford RJ. Performance theory of diagonal conducting wall magnetohydrodynamic accelerators. *Journal of Propulsion and Power*. 2004; 20: 742-750. Available from: <https://doi.org/10.2514/1.3698>.
- [97] Litchford R. Performance theory of diagonal conducting wall MHD accelerators. In: *34th AIAA Plasmadynamics and Lasers Conference*. Orlando, Florida, USA: AIAA; 2003. Available from: <https://doi.org/10.2514/6.2003-4284>.
- [98] Veefkind A, Blom JH, Rietjens LHTh. *Theoretical and experimental investigation of a non-equilibrium plasma in a MHD channel*. Eindhoven, Netherlands: Technische Hogeschool Eindhoven; 1968. Available from: <https://research.tue.nl/en/publications/theoretical-and-experimental-investigation-of-a-non-equilibrium-p> [Accessed 23rd March 2025].
- [99] Anwari M, Sakamoto N, Hardianto T, Kondo J, Harada N. Numerical analysis of magnetohydrodynamic accelerator performance with diagonal electrode connection. *Energy Conversion and Management*. 2006; 47: 1857-1867. Available from: <https://doi.org/10.1016/j.enconman.2005.10.008>.
- [100] Chandra A, Bhadoria BS, Verma SS. Performance of a MHD retrofit channel with diagonal electrode geometry. *Energy Conversion and Management*. 1996; 37: 311-317. Available from: [https://doi.org/10.1016/0196-8904\(95\)00182-4](https://doi.org/10.1016/0196-8904(95)00182-4).
- [101] Hardianto T, Sakamoto N, Harada N. Study of a diagonal channel MHD power generation. In: *45th AIAA Aerospace Sciences Meeting and Exhibit*. Reno, Nevada, USA: AIAA; 2007. Available from: <https://doi.org/10.2514/6.2007-398>.
- [102] Marzouk OA. Detailed and simplified plasma models in combined-cycle magnetohydrodynamic power systems. *International Journal of Advanced and Applied Sciences*. 2023; 10: 96-108. Available from: <https://doi.org/10.21833/ijaas.2023.11.013>.
- [103] Marzouk OA. Estimated electric conductivities of thermal plasma for air-fuel combustion and oxy-fuel combustion with potassium or cesium seeding. *Heliyon*. 2024; 10: e31697. Available from: <https://doi.org/10.1016/j.heliyon.2024.e31697>.

- [104] Banda HJ, Nzabanimana J. Effect of integrating physics education technology simulations on students' conceptual understanding in physics: A review of literature. *Physical Review Physics Education Research*. 2021; 17: 023108. Available from: <https://doi.org/10.1103/PhysRevPhysEducRes.17.023108>.
- [105] Velikhov EP, Pismenny VD, Matveenko OG, Panchenko VP, Yakushev AA, Pisakin AV, et al. Pulsed MHD power system "Sakhalin" - The world largest solid propellant fueled MHD generator of 500 MWe electric power output. In: *13th International Conference on MHD Electrical Power Generation and High Temperature Technologies*. Beijing, China; 1999. p.387-398.
- [106] Khrapak SA, Khrapak AG. On the conductivity of moderately non-ideal completely ionized plasma. *Results in Physics*. 2020; 17: 103163. Available from: <https://doi.org/10.1016/j.rinp.2020.103163>.
- [107] Sheridan TE, Goree JA. Analytic expression for the electric potential in the plasma sheath. *IEEE Transactions on Plasma Science*. 1989; 17: 884-888. Available from: <https://doi.org/10.1109/27.41228>.
- [108] Novikov GG, Tsygankov SF. Reflection of radio waves from a meteor trail containing two kinds of ions. *Radiophysics and Quantum Electronics*. 1981; 24: 979-984. Available from: <https://doi.org/10.1007/BF01034305>.
- [109] Lucquin-Desreux B. Diffusion of electrons by multicharged ions. *Mathematical Models and Methods in Applied Sciences*. 2000; 10: 409-440. Available from: <https://doi.org/10.1142/S0218202500000240>.
- [110] Yang Z, Chen R. A theory about induced electric current and heating in plasma. *Natural Science*. 2011; 3: 275-284. Available from: <https://doi.org/10.4236/ns.2011.34035>.
- [111] Knaepen B, Moreau R. Magnetohydrodynamic turbulence at low magnetic reynolds number. *Annual Review of Fluid Mechanics*. 2008; 40: 25-45. Available from: <https://doi.org/10.1146/annurev.fluid.39.050905.110231>.
- [112] Lee D, Choi H. Magnetohydrodynamic turbulent flow in a channel at low magnetic Reynolds number. *Journal of Fluid Mechanics*. 2001; 439: 367-394. Available from: <https://doi.org/10.1017/S0022112001004621>.
- [113] Davidson PA. *An Introduction to Magnetohydrodynamics*. Cambridge University Press; USA; 2001.
- [114] Rosa RJ, Krueger CH, Shioda S. Plasmas in MHD power generation. *IEEE Transactions on Plasma Science*. 1991; 19: 1180-1190. Available from: <https://doi.org/10.1109/27.125040>.
- [115] Khan O, Hoffmann K, Dietiker JF. Validity of low magnetic reynolds number formulation of magnetofluidynamics. In: *38th Plasmadynamics and Lasers Conference*. Miami, Florida, USA: AIAA; 2007. Available from: <https://doi.org/10.2514/6.2007-4374>.
- [116] van Oeveren SB, Gildfind D, Wheatley V, Gollan R, Jacobs P. Numerical study of magnetic field deformation for a blunt body with an applied magnetic field during atmospheric entry. In: *AIAA SCITECH 2024 Forum*. Orlando, Florida, USA: AIAA; 2024. Available from: <https://doi.org/10.2514/6.2024-1646>.
- [117] Maxwell CD, Demetriades ST. Initial tests of a lightweight, self-excited MHD power generator. *Journal of Propulsion and Power*. 1986; 2: 474-480. Available from: <https://doi.org/10.2514/3.22931>.
- [118] Quirino TS, Verissimo GL, Colaço MJ. Numerical analysis of a MHD generator with helical geometry. *Computational Thermal Sciences*. 2022; 14: 19-37. Available from: <https://doi.org/10.1615/ComputThermalScien.2022042038>.
- [119] Smolentsev S, Cuevas S, Beltrán A. Induced electric current-based formulation in computations of low magnetic Reynolds number magnetohydrodynamic flows. *Journal of Computational Physics*. 2010; 229: 1558-1572. Available from: <https://doi.org/10.1016/j.jcp.2009.10.044>.
- [120] Bordes C, Brito D, Garambois S, Holzhauer J, Jouniaux L, Dietrich M. Laboratory measurements of coseismic fields. In: *Seismoelectric Exploration*. American Geophysical Union (AGU); 2020. p.109-122. Available from: <https://doi.org/10.1002/9781119127383.ch7>.
- [121] Umoh IJ, Kazmierski TJ, Al-Hashimi BM. A dual-gate graphene FET model for circuit simulation–SPICE implementation. *IEEE Transactions on Nanotechnology*. 2013; 12: 427-435. Available from: <https://doi.org/10.1109/TNANO.2013.2253490>.
- [122] Frost LS. Conductivity of seeded atmospheric pressure plasmas. *Journal of Applied Physics*. 1961; 32: 2029-2036. Available from: <https://doi.org/10.1063/1.1728283>.
- [123] Freck DV. On the electrical conductivity of seeded air combustion products. *British Journal of Applied Physics*. 1964; 15: 301-310. Available from: <https://doi.org/10.1088/0508-3443/15/3/309>.
- [124] Blackman VH, Jones MS Jr, Demetriades A. MHD power generation studies in rectangular channels. In: *Proceedings of the 2nd Symposium on the Engineering Aspects of Magnetohydrodynamics (EAMHD-2)*. Columbia University Press; 1961. p.180-210.

- [125] Klepeis JE, Hruby V. *Development Program for MHD Power Generation. Disk Generator Performance*. Avco-Everett Research Lab., Inc.; 1977. Available from: <https://doi.org/10.2172/6175601>.
- [126] Medin SA. Magnetohydrodynamic electrical power generators. In: *Thermopedia*. Begel House Inc.; 2011. Available from: https://doi.org/10.1615/AtoZ.m.magnetohydrodynamic_electrical_power_generators.
- [127] Eraslan AH. Temperature distributions in MHD channels with Hall effect. *AIAA Journal*. 1969; 7: 186-188. Available from: <https://doi.org/10.2514/3.5072>.
- [128] Wu YCL, Dicks JB, Denzel DL, Witkowski S, Shanklin RV, Zitzow U, et al. MHD generator in two-terminal operation. *AIAA Journal*. 1968; 6: 1651-1657. Available from: <https://doi.org/10.2514/3.4841>.
- [129] Grandi G, Kazimierczuk MK, Massarini A, Reggiani U, Sancineto G. Model of laminated iron-core inductors for high frequencies. *IEEE Transactions on Magnetics*. 2004; 40: 1839-1845. Available from: <https://doi.org/10.1109/TMAG.2004.830508>.
- [130] Magdaleno-Adame S, Kefalas TD, Garcia-Martinez S, Perez-Rojas C. Electromagnetic finite element analysis of electrical steels combinations in lamination core steps of single-phase distribution transformers. In: *2017 IEEE International Autumn Meeting on Power, Electronics and Computing (ROPEC)*. Ixtapa, Mexico: IEEE; 2017. p.1-5. Available from: <https://doi.org/10.1109/ROPEC.2017.8261585>.
- [131] Moses AJ, Pegler SM. The effects of flexible bonding of laminations in a transformer core. *Journal of Sound and Vibration*. 1973; 29: 103-112. Available from: [https://doi.org/10.1016/S0022-460X\(73\)80129-4](https://doi.org/10.1016/S0022-460X(73)80129-4).
- [132] Kien LC. Numerical calculations and analyses in diagonal type MHD generator. *Vietnam Journal of Science and Technology*. 2014; 52: 701-710. Available from: <https://doi.org/10.15625/0866-708X/52/6/2603>.
- [133] Komatsu F, Tanaka M, Murakami T, Okuno Y. Experiments on high-temperature inert gas plasma MHD electrical power generation with hall and diagonal connections. *Electrical Engineering in Japan*. 2015; 193: 17-23. Available from: <https://doi.org/10.1002/eej.22761>.
- [134] Hardianto T, Sakamoto N, Harada N. Three dimensional flow analyses in a diagonal type MHD generator. *American Journal of Applied Sciences*. 2006; 3: 1973-1978. Available from: <https://doi.org/10.3844/ajassp.2006.1973.1978>.
- [135] Bussière W, Duffour E, André P, Pellet R, Brunet L. Experimental assessment of temperature in plasma wall interaction. *European Physical Journal D*. 2004; 28: 79-90. Available from: <https://doi.org/10.1140/epjd/e2003-00286-2>.
- [136] Fujino T, Ichinokiyama D, Ichikawa T. Plasma characteristics and performance of nonequilibrium disk magnetohydrodynamic generator with swirl vanes. *Journal of Propulsion and Power*. 2018; 34: 992-1001. Available from: <https://doi.org/10.2514/1.B36947>.
- [137] Lee GH, Kim HR. Numerical study of Faraday-type nitrogen plasma magnetohydrodynamic generator. *Journal of the Korean Physical Society*. 2021; 78: 600-606. Available from: <https://doi.org/10.1007/s40042-021-00116-z>.
- [138] Doss ED, Picologlou BF. Interelectrode resistance and performance of small- and large-scale MHD generators. *Journal of Energy*. 1983; 7: 454-455. Available from: <https://doi.org/10.2514/3.62682>.
- [139] Kominami S, Fujino T, Ishikawa M, Okuno Y. Performance characteristics of commercial scale disk MHD generator with plasma production technique. In: *40th AIAA Plasmadynamics and Lasers Conference*. San Antonio, Texas, USA: AIAA; 2009. Available from: <https://doi.org/10.2514/6.2009-3826>.
- [140] Levi E. Power: MHD's target: Payoff by 2000: Efficiencies over 50 percent and generating costs of 32 mills/kWh may make magnetohydrodynamic systems viable by 1995. *IEEE Spectrum*. 1978; 15: 46-51. Available from: <https://doi.org/10.1109/MSPEC.1978.6367698>.
- [141] Meena L, Niranjana MS, Aman, Gautam, Gagandeep, Kumar G, et al. Numerical study of convergent-divergent nozzle at different throat diameters and divergence angles. *Materials Today: Proceedings*. 2021; 46: 10676-10680. Available from: <https://doi.org/10.1016/j.matpr.2021.01.432>.
- [142] Kamali R, Binesh AR. The importance of sensitive parameters effect on the combustion in a high velocity oxygen-fuel spray system. *International Communications in Heat and Mass Transfer*. 2009; 36: 978-983. Available from: <https://doi.org/10.1016/j.icheatmasstransfer.2009.06.015>.
- [143] Zhou R, Wang JP. Numerical investigation of shock wave reflections near the head ends of rotating detonation engines. *Shock Waves*. 2013; 23: 461-472. Available from: <https://doi.org/10.1007/s00193-013-0440-0>.
- [144] Oka T, Itoh Y, Yanagi Y, Yoshikawa M, Ikuta H, Mizutani U. Construction of a 2-5 T class superconducting magnetic field generator with use of an Sm123 bulk superconductor and its application to high-magnetic field demanding devices. *Physica C: Superconductivity*. 2000; 335: 101-106. Available from: [https://doi.org/10.1016/S0921-4534\(00\)00152-0](https://doi.org/10.1016/S0921-4534(00)00152-0).

- [145] Fujishiro H, Tateiwa T, Fujiwara A, Oka T, Hayashi H. Higher trapped field over 5T on HTSC bulk by modified pulse field magnetizing. *Physica C: Superconductivity and Its Applications*. 2006; 445-448: 334-338. Available from: <https://doi.org/10.1016/j.physc.2006.04.077>.
- [146] Raymond S, Ressouche E, Knebel G, Aoki D, Flouquet J. Magnetic structure of CeRhIn₅ under magnetic field. *Journal of Physics: Condensed Matter*. 2007; 19: 242204. Available from: <https://doi.org/10.1088/0953-8984/19/24/242204>.
- [147] Wang Q, Dai Y, Ni Z, Cheng S, Wen G, Hu X, et al. High magnetic field superconducting magnet system up to 25 T for ExCES. *IEEE Transactions on Applied Superconductivity*. 2013; 23: 4300905. Available from: <https://doi.org/10.1109/TASC.2012.2236376>.
- [148] Kirby GA, van Nugteren J, Ballarino A, Bottura L, Chouika N, Clement S, et al. Accelerator-quality HTS dipole magnet demonstrator designs for the EuCARD-2 5-T 40-mm clear aperture magnet. *IEEE Transactions on Applied Superconductivity*. 2015; 25: 1-5. Available from: <https://doi.org/10.1109/TASC.2014.2361933>.
- [149] Loening NM, Rosay M, Weis V, Griffin RG. Solution-state dynamic nuclear polarization at high magnetic field. *Journal of the American Chemical Society*. 2002; 124: 8808-8809. Available from: <https://doi.org/10.1021/ja026660g>.
- [150] Mlodik ME, Kolmes EJ, Ochs IE, Fisch NJ. Generalized impurity pinch in partially magnetized multi-ion plasma. *Physics of Plasmas*. 2021; 28: 052702. Available from: <https://doi.org/10.1063/5.0046603>.
- [151] Rosenbaum M, Shamma SE, Louis JF. Experimental and theoretical studies of the effects of nonuniformities in equilibrium MHD generators. In: *International Conference on MHD Electrical Power Generation*. Cambridge, Massachusetts, USA; 1980. p.1-9. Available from: <https://www.osti.gov/biblio/5491766> [Accessed 10th May 2025].
- [152] Yamasaki H, Shioda S. MHD power generation with fully ionized seed. *Journal of Energy*. 1977; 1: 301-305. Available from: <https://doi.org/10.2514/3.47944>.
- [153] Nakamura T, Riedmuller W. Stability of nonequilibrium MHD plasma in the regime of fully ionized seed. *AIAA Journal*. 1974; 12: 661-668. Available from: <https://doi.org/10.2514/3.49316>.
- [154] Tsunoda K, Kariya K, Suekane T, Yamasaki H, Okamura T, Harada N, et al. High-enthalpy extraction experiments with disk MHD generators. *JSME International Journal Series B*. 1995; 38: 265-272. Available from: <https://doi.org/10.1299/jsmeb.38.265>.
- [155] Feldman L, Burkhalter J. Numerical solutions of transient aerodynamic and MHD phenomena. In: *11th Fluid and Plasma Dynamics Conference*. Seattle, Washington, USA: AIAA; 1978. Available from: <https://doi.org/10.2514/6.1978-1176>.
- [156] Marzouk OA. Hydrogen utilization as a plasma source for magnetohydrodynamic direct power extraction (MHD-DPE). *IEEE Access*. 2024; 12: 167088-167107. Available from: <https://doi.org/10.1109/ACCESS.2024.3496796>.
- [157] Marzouk OA. Urban air mobility and flying cars: Overview, examples, prospects, drawbacks, and solutions. *Open Engineering*. 2022; 12: 662-679. Available from: <https://doi.org/10.1515/eng-2022-0379>.
- [158] Stickler DB, DeSaro R. Slag interaction phenomena on MHD generator electrodes. *Journal of Energy*. 1977; 1: 169-179. Available from: <https://doi.org/10.2514/3.62326>.
- [159] Yoshida M, Umoto J. Influences of coal slag on electrical characteristics of a Faraday MHD generator. *Energy Conversion and Management*. 1989; 29: 217-226. Available from: [https://doi.org/10.1016/0196-8904\(89\)90007-1](https://doi.org/10.1016/0196-8904(89)90007-1).
- [160] Wang XH, Zhao DQ, He LB, Jiang LQ, He Q, Chen Y. Modeling of a coal-fired slagging combustor: Development of a slag submodel. *Combustion and Flame*. 2007; 149: 249-260. Available from: <https://doi.org/10.1016/j.combustflame.2007.02.001>.
- [161] Chen L, Yong SZ, Ghoniem AF. Modeling the slag behavior in three dimensional CFD simulation of a vertically-oriented oxy-coal combustor. *Fuel Processing Technology*. 2013; 112: 106-117. Available from: <https://doi.org/10.1016/j.fuproc.2013.02.010>.
- [162] Agee FJ, Lehr FM, Vigil M, Kaye R, Gaudet J, Shiffler D. Explosively-driven magnetohydrodynamic (MHD) generator studies. In: *Digest of Technical Papers. Tenth IEEE International Pulsed Power Conference*. IEEE; 1995. p.1068-1073. Available from: <https://doi.org/10.1109/PPC.1995.599755>.
- [163] Takahashi T, Fujino T, Ishikawa M. Comparison of generator performance of small-scale MHD generators with different electrode dispositions and load connection systems. *Journal of International Council on Electrical Engineering*. 2014; 4: 192-198. Available from: <https://doi.org/10.5370/JICEE.2014.4.3.192>.
- [164] Messerle HK. *Magnetohydrodynamic Electrical Power Generation*. Chichester, England, UK: Wiley; 1995.

- [165] Murakami T, Okuno Y. Experiment and simulation of MHD power generation using convexly divergent channel. In: *42nd AIAA Plasmadynamics and Lasers Conference*. Honolulu, Hawaii, USA: AIAA; 2011. Available from: <https://doi.org/10.2514/6.2011-3287>.
- [166] Swallom DW, Goldfarb VM, Gibbs JS, Sadovnik I, Zeigarnik VA, Kuzmin RK, et al. Results from the Pamir-3U pulsed portable MHD power system program. In: *12th International Conference on MHD Electrical Power Generation*. Yokohama, Japan; 1996. p.186-195.
- [167] Sugita H, Matsuo T, Inui Y, Ishikawa M. Two-dimensional analysis of gas-particle two phase flow in pulsed MHD channel. In: *30th Plasmadynamic and Lasers Conference*. Norfolk, Virginia, USA: American Institute of Aeronautics and Astronautics; 1999. Available from: <https://doi.org/10.2514/6.1999-3483>.
- [168] Koshiba Y, Yuhara M, Ishikawa M. Two-dimensional analysis of effects of induced magnetic field on generator performance of a large-scale pulsed MHD generator. In: *35th AIAA Plasmadynamics and Lasers Conference*. Portland, Oregon, USA: AIAA; 2004. Available from: <https://doi.org/10.2514/6.2004-2368>.
- [169] Chejarla VS, Ahmed S, Belz J, Scheunert J, Beyer A, Volz K. Measuring spatially-resolved potential drops at semiconductor hetero-interfaces using 4D-STEM. *Small Methods*. 2023; 7: 2300453. Available from: <https://doi.org/10.1002/smt.202300453>.
- [170] Sutton GW, Sherman A. *Engineering Magnetohydrodynamics*. Mineola, New York, USA: Courier Dover Publications; 2006. Available from: <https://books.google.com.om/books?id=yJaRDQAAQBAJ> [Accessed 19th March 2025].
- [171] Sakamoto N, Harada N. Three-dimensional computational study on a magnetohydrodynamic accelerator in hall current neutralized condition. *IEEJ Transactions on Fundamentals and Materials*. 2008; 128: 343-349. Available from: <https://doi.org/10.1541/ieejfms.128.343>.
- [172] Marshak AH, van Vliet KM. Electrical current in solids with position-dependent band structure. *Solid-State Electronics*. 1978; 21: 417-427. Available from: [https://doi.org/10.1016/0038-1101\(78\)90272-1](https://doi.org/10.1016/0038-1101(78)90272-1).
- [173] Nakachai R, Poonsawat S, Sutthinet C, Ruangphanit A, Poyai A, Phetchakul T. Horizontal magnetic field MAGFET by conventional MOSFET structure. In: *2018 International Electrical Engineering Congress (iEECON)*. Krabi, Thailand: IEEE; 2018. p.1-4. Available from: <https://doi.org/10.1109/IEECON.2018.8712249>.
- [174] Kobayashi D, Aimi M, Saito H, Hirose K. Time-domain component analysis of heavy-ion-induced transient currents in fully-depleted SOI MOSFETs. *IEEE Transactions on Nuclear Science*. 2006; 53: 3372-3378. Available from: <https://doi.org/10.1109/TNS.2006.886234>.
- [175] Menart J, Shang J, Hayes J. Development of a Langmuir probe for plasma diagnostic work in high speed flow. In: *32nd AIAA Plasmadynamics and Lasers Conference*. Anaheim, California, USA: AIAA; 2001. Available from: <https://doi.org/10.2514/6.2001-2804>.
- [176] Ishida K, Tashiro S, Nomura K, Wu D, Tanaka M. Elucidation of arc coupling mechanism in plasma-MIG hybrid welding process through spectroscopic measurement of 3D distributions of plasma temperature and iron vapor concentration. *Journal of Manufacturing Processes*. 2022; 77: 743-753. Available from: <https://doi.org/10.1016/j.jmapro.2022.04.002>.
- [177] Ochoa Brezmes A, Bretkopf C. Simulation of inductively coupled plasma with applied bias voltage using COMSOL. *Vacuum*. 2014; 109: 52-60. Available from: <https://doi.org/10.1016/j.vacuum.2014.06.012>.
- [178] United States National Institute of Standards and Technology (NIST). *CODATA Value: Elementary Charge*. 2025. Available from: <https://physics.nist.gov/cgi-bin/cuu/Value?e> [Accessed 20th March 2025].
- [179] National Instruments (NI). *NI: Elementary Charge Constant*. 2023. Available from: <https://www.ni.com/docs/en-US/bundle/labview-nxg-nodes-api-ref/page/elementary-charge.html> [Accessed 20th March 2025].
- [180] Jeckelmann B, Piquemal F. The elementary charge for the definition and realization of the ampere. *Annalen der Physik*. 2019; 531: 1800389. Available from: <https://doi.org/10.1002/andp.201800389>.
- [181] MacDonald AH, Rice TM, Brinkman WF. Hall voltage and current distributions in an ideal two-dimensional system. *Physical Review B*. 1983; 28: 3648-3650. Available from: <https://doi.org/10.1103/PhysRevB.28.3648>.
- [182] Terasawa T. Hall current effect on tearing mode instability. *Geophysical Research Letters*. 1983; 10: 475-478. Available from: <https://doi.org/10.1029/GL010i006p00475>.
- [183] Khan M, Maqbool K, Hayat T. Influence of Hall current on the flows of a generalized Oldroyd-B fluid in a porous space. *Acta Mechanica*. 2006; 184: 1-13. Available from: <https://doi.org/10.1007/s00707-006-0326-7>.
- [184] Litchford RJ, Cole JW, Lineberry JT, Chapman JN, Schmidt HJ, Lineberry CW. *Magnetohydrodynamic Augmented Propulsion Experiment: I. Performance Analysis and Design*. Alabama, USA: NASA, Marshall Space

- Flight Center; 2003. Available from: <https://ntrs.nasa.gov/api/citations/20030025730/downloads/20030025730.pdf> [Accessed 19th March 2025].
- [185] Bogdanoff D, Mehta U. Experimental demonstration of MHD acceleration. In: *34th AIAA Plasmadynamics and Lasers Conference*. Orlando, Florida, USA: AIAA; 2003. Available from: <https://doi.org/10.2514/6.2003-4285>.
- [186] Brogan T. The 20MW LORHO MHD accelerator for wind tunnel drive - Design, construction and critique. In: *30th Plasmadynamic and Lasers Conference*. Norfolk, Virginia, USA: AIAA; 1999. Available from: <https://doi.org/10.2514/6.1999-3720>.
- [187] Angrist SW. *Direct Energy Conversion*. 4th ed. Boston, Massachusetts, USA: Allyn and Bacon; 1982.
- [188] Israelevich PL, Gombosi TI, Ershkovich AI, DeZeeuw DL, Neubauer FM, Powell KG. The induced magnetosphere of comet Halley: 4. Comparison of in situ observations and numerical simulations. *Journal of Geophysical Research: Space Physics*. 1999; 104: 28309-28319. Available from: <https://doi.org/10.1029/1999JA900371>.
- [189] Marzouk OA. Flow control using bifrequency motion. *Theoretical and Computational Fluid Dynamics*. 2011; 25: 381-405. Available from: <https://doi.org/10.1007/s00162-010-0206-6>.
- [190] Marzouk OA. Contrasting the Cartesian and polar forms of the shedding-induced force vector in response to 12 subharmonic and superharmonic mechanical excitations. *Fluid Dynamics Research*. 2010; 42: 035507. Available from: <https://doi.org/10.1088/0169-5983/42/3/035507>.
- [191] Aithal SM. Characteristics of optimum power extraction in a MHD generator with subsonic and supersonic inlets. *Energy Conversion and Management*. 2009; 50: 765-771. Available from: <https://doi.org/10.1016/j.enconman.2008.09.037>.
- [192] Liberati A, Okuno Y. Improvement of Plasma-flow behavior and performance of a disk MHD generator under high magnetic flux densities. *IEEE Transactions on Power and Energy*. 2008; 128: 493-498. Available from: <https://doi.org/10.1541/ieejpes.128.493>.
- [193] Kaneko K, Oyama A, Yakeno A, Hamada S. Mach number effect on the drag reducing performance of the riblet in the transition and turbulent flow. In: *AIAA SCITECH 2024 Forum*. Orlando, Florida, USA: AIAA; 2024. Available from: <https://doi.org/10.2514/6.2024-0890>.
- [194] Georgiadis NJ, Wernet MP, Locke RJ, Eck DG. Mach number and heating effects on turbulent supersonic jets. *AIAA Journal*. 2024; 62: 31-51. Available from: <https://doi.org/10.2514/1.J063186>.
- [195] Benyahia S. A time-averaged model for gas-solids flow in a one-dimensional vertical channel. *Chemical Engineering Science*. 2008; 63: 2536-2547. Available from: <https://doi.org/10.1016/j.ces.2008.02.012>.
- [196] Ercan A, Kavvas ML. Time-space fractional governing equations of one-dimensional unsteady open channel flow process: Numerical solution and exploration. *Hydrological Processes*. 2017; 31: 2961-2971. Available from: <https://doi.org/10.1002/hyp.11240>.
- [197] Gąsiorowski D, Napiórkowski JJ, Szymkiewicz R. One-dimensional modeling of flows in open channels. In: Rowiński P, Radecki-Pawlik A. (eds.) *Rivers - Physical, Fluvial and Environmental Processes*. Cham: Springer International Publishing; 2015. p.137-167. Available from: https://doi.org/10.1007/978-3-319-17719-9_6.
- [198] Boeck T, Brynjell-Rahkola M, Duguet Y. Energy stability analysis of MHD flow in a rectangular duct. *Proceedings in Applied Mathematics and Mechanics*. 2024; 24: e202400041. Available from: <https://doi.org/10.1002/pamm.202400041>.
- [199] Núñez M. Generalized Ohm's law and geometric optics: Applications to magnetosonic waves. *International Journal of Non-Linear Mechanics*. 2019; 110: 21-25. Available from: <https://doi.org/10.1016/j.ijnonlinmec.2019.01.007>.
- [200] Velikhov EP, Golubev VS, Dykhne AM. *Physical Phenomena in a Low-Temperature Non-Equilibrium Plasma and in MHD Generators with Generators with Non-Equilibrium Conductivity*. Vienna, Austria: IAEA; 1976. Available from: <https://inis.iaea.org/records/e28xk-19082/files/53066451.pdf> [Accessed 20th March 2025].
- [201] Marzouk OA. Benchmarks for the Omani higher education students-faculty ratio (SFR) based on World Bank data, QS rankings, and THE rankings. *Cogent Education*. 2024; 11: 231711. Available from: <https://doi.org/10.1080/2331186X.2024.2317117>.
- [202] Marzouk OA. Power density and thermochemical properties of hydrogen magnetohydrodynamic (H2MHD) generators at different pressures, seed types, seed levels, and oxidizer. *Hydrogen*. 2025; 6: 31. Available from: <https://doi.org/10.3390/hydrogen6020031>.